AALTO UNIVERSITY

School of Science and Technology

Faculty of Electronics, Communications and Automation

Department of Radio Science and Engineering

Matti Vaaja

Design and Realisation of L-band Frequency Scanning Radiometer

The thesis was submitted in partial fulfillment for the degree of Licentiate in Technology, ___.___._____

Supervisor	Prof. Antti Räisänen
Instructor	Dr. Juha Mallat
Second examiner	Dr. Andreas Colliander

AALTO UNIVERSITY   ABSTRACT OF THE
SCHOOL OF SCIENCE AND TECHNOLOGY   LICENTIATE'S THESIS

Author:	Matti Vaaja
Title of thesis:	Design and Realisation of L-band Frequency Scanning Radiometer
Date:	24.3.2010 **Number of pages**: 73

Department:	Department of Radio Science and Engineering
Chair:	S-26 Radio Engineering

Supervisor:	Prof. Antti Räisänen
Instructor:	Dr. Juha Mallat
Second examiner:	Dr. Andreas Colliander

L-band (1-2 GHz) radiometry has been an ongoing research topic in the Department of Radio Science and Engineering for a number of years. In addition to remote sensing and radioastronomy applications, a radiometer can be used for detecting unwanted radio emissions in a protected frequency band.

A frequency scanning radiometer (FIRaL) for detecting radio interference at the frequency interval of 1920 – 1980 MHz is designed and realised in this Licentiate thesis work. The aforementioned frequency band is reserved for mobile communication applications. The theory of radiometry is presented to the necessary extent in order to facilitate the FIRaL radiometer design. The design of the receiver and local oscillator electronics and pyramidal horn antenna is presented.

Radiometer performance is studied by measuring the relevant device parameters in laboratory conditions. The feasibility of the radiometer to perform real-world interference surveys is tested by on-site measurements. The realised radiometer receiver input noise temperature is 661 ± 58 K or better. The radiometer is deemed suitable for interference measurements. The preliminary on-site measurements suggests that further measurements are feasible in order to study the extent of radio emissions in the 1920 – 1980 MHz mobile communications band.

Key words: Radiometer, radio interference, RF design, calibration

AALTO-YLIOPISTO   LISENSIAATINTUTKIMUKSEN
TEKNILLINEN KORKEAKOULU   TIIVISTELMÄ

Tekijä:	Matti Vaaja	
Työn nimi:	L-alueen taajuuspyyhkäisevän radiometrin suunnittelu ja toteutus	
Päiväys:	24.3.2010	**Sivujen lukumäärä**: 73
Laitos:	Radiotieteen ja –tekniikan laitos	
Professuuri:	S-26 Radiotekniikka	
Työn valvoja:	Prof. Antti Räisänen	
Työn ohjaaja:	TkT Juha Mallat	
Työn toinen tarkastaja:	TkT Andreas Colliander	

Radiotieteen ja –tekniikan laitoksella on jo useita vuosia tutkittu L-alueen (1-2 GHz) radiometriasovelluksia. Kaukokartoituksen ja radioastronomian ohella radiometreillä voidaan tutkia radiotaajuisia häiriöitä suojatuilla taajuusalueilla.

Tässä työssä on suunniteltu ja toteutettu L-alueen taajuuspyyhkäisevä radiometri (FIRaL) 1920-1980 MHz:in taajuusalueelta mahdollisesti löytyvien radiotaajuisten häiriöiden tutkimiseen. Edellä mainittu taajuuskaista on varattu matkaviestintäsovellusten käyttöön. Radiometria esitellään FIRaL radiometrin suunnittelun taustatiedoksi tarvittavalla laajuudella. Vastaanottimen ja paikallisoskillaattorin elektroniikan ja pyramiditorviantennin suunnittelu esitellään.

Radiometrin suorituskykyä tutkitaan mittaamalla kyseisen laitteen parametrit laboratorio-olosuhteissa. Radiometrin soveltuvuus käytännön häiriömittauksiin testataan tekemällä mittauksia tyypillisessä matkaviestintätukiaseman sijaintipaikassa. Rakennetun radiometrin kohinalämpötila on maksimissaan 661 ± 58 K. Radiometri todetaan käyttökelpoiseksi häiriömittauksiin. Alustavista mittauksista löytyi todennäköisiä häiriölähteitä 1920 – 1980 MHz matkaviestintäkaistalta ja lisätutkimukset häiriöiden laajempaan kartoitukseen ovat perusteltuja.

Avainsanat: Radiometri, radiotaajuiset häiriöt, RF-suunnittelu, kalibrointi

Contents

Preface

Espoo, xx.xx.xxxx

Matti Vaaja

Abbreviations

ACL	Active cold load
ADC	Analog-to-digital conversion
AUT	Antenna under test
CNS	Central noise source
ESA	European Space Agency
FICORA	Finnish Communications Regulatory Authority
FIRaL	L-band frequency scanning radiometer
IC	Integrated circuit
IF	Intermediate frequency
LIME	L-band Interference Measurements in Urban and Suburban Environment
LO	Local oscillator
NSN	Nokia Siemens Networks Oy
PC	Personal computer
PCB	Printed circuit board
PMS	Total power measurement
RCB	Receiver control board
RF	Radio frequency
RMS	Root-mean-square
RSS	Root-sum-square
RX	Radio receiver
SAW	Surface acoustic wave
SMD	Surface mount device
SMOS	Soil Moisture and Ocean Salinity
SNR	Signal-to-noise ratio
TCB	Thermal control board
Tekes	Finnish Funding Agency for Technology and Innovation
TKK	Teknillinen korkeakoulu
TTL	Transistor-transistor logic
UMTS	Universal Mobile Telecommunications System
W-CDMA	Wideband Code Division Multiple Access

List of Symbols

A_r	antenna effective area
A	horn aperture H-plane dimension
B	bandwidth
B	horn aperture E-plane dimension
$B(\theta,\varphi)$	gray body brightness
B_{bb}	blackbody brightness
B_f	blackbody spectral brightness
B_{mb}	antenna main beam direction brightness
B_{RF}	RF-amplifier bandwidth
c	velocity of light
C	capacitance
C_d	square-law detector power-sensitivity constant
D	directivity
f	frequency
$f_{crystal}$	crystal oscillator frequency
f_{IF}	intermediate frequency
f_{LO}	local oscillator frequency
f_{ref}	PLL reference frequency
f_{RF}	radio frequency
f_S	Dicke switch modulation frequency
F	noise figure
g	radiometer total gain
g_{LF}	low-pass filter gain
G	gain
G_a	antenna gain
G_n	normalised antenna directivity
G_{ref}	reference antenna gain
h	Planck's constant
j	imaginary unit
k	Boltzmann's constant
L	loss factor
L	inductance
L_c	cable loss per segment
n	index

N	integer number
P_a	received power level with AUT
P_{no}	output noise power
P_{ref}	received power level with reference antenna
R	horn antenna depth
R_G	noise generator reflection coefficient
R_L	load resistance
R_R	receiver input reflection coefficient
R_{1S}	port 1 reflection coefficient
R_{2S}	port 2 reflection coefficient
s	E-plane quadratic phase distribution constant
t	H-plane quadratic phase distribution constant
T	absolute temperature
T_A	antenna radiometric temperature
$T_A^{'}$	antenna temperature of a lossy antenna
$T_{AP}(\theta,\varphi)$	apparent temperature distribution
$T_B(\theta,\varphi)$	brightness temperature
T_c	cold calibration load noise temperature
T_E	effective input noise temperature
T_G	noise generator temperature
T_h	hot calibration load noise temperature
T_I	injected excess noise temperature
T_{IN}	noise temperature of the net power delivered to the receiver
T_{LN}	liquid nitrogen boiling temperature
T_n	cable segment temperature
T_N	noise temperature
T_{phys}	physical temperature
T_R	receiver backward radiation noise temperature
T_{REC}	radiometer noise temperature
$T_{REC}^{'}$	transmission line - receiver cascade effective input noise temperature
T_{REF}	reference load temperature
T_{SYS}	effective system input noise temperature
T_0	standardised physical temperature
V_d	detector output voltage
V_{out}	radiometer output voltage

$\bar{V}_{out}$	radiometer DC output voltage	
V_0	detector offset	
x	normalised reactance	
X_L	load reactance	
Z_L	load impedance	
Z_0	transmission line characteristic impedance	
Z_{01}	port 1 impedance	
Z_{02}	port 2 impedance	
$\varepsilon(\theta,\varphi)$	emissivity	
Δf	bandwidth	
ΔG	gain fluctuation	
ΔT	radiometer measurement uncertainty	
ΔT	radiometer sensitivity	
ΔT_G	radiometer measurement uncertainty due to gain fluctuation	
Γ	mismatch loss factor	
ε_r	effective electrical permittivity	
η_l	antenna radiation efficiency	
θ	angle	
θ_{az}	beamwidth in azimuth direction	
θ_{el}	beamwidth in elevation direction	
λ	wavelength	
ρ_a	antenna reflection coefficient	
ρ_{HP}	power meter reflection coefficient	
ρ_{IF}	IF section output reflection coefficient	
ρ_{LO}	LO output port reflection coefficient	
ρ_S	signal generator reflection coefficient	
τ	integration time	
T	transmission factor	
ω	angular frequency	
Ω_p	pattern solid angle	
Ω_t	transmitting antenna solid angle	

1 Introduction

Electromagnetic spectrum is a limited resource like land and water. Government bodies are therefore constantly monitoring and allocating frequency bands for specific usage. European Communications Office [1] regulates frequency usage on a continent wide basis. Nationally, the Finnish Communications Regulatory Authority (FICORA) is responsible for dividing the radio spectrum for different users and applications. According to the Radio Frequency Regulation 4, issued on the 4th of November 2009 by FICORA, the frequency interval of 1920-1980 MHz in the L-band (1-2 GHz) is reserved for International Mobile Telecommunications and specifically for the Universal Mobile Telecommunications System (UMTS) base station receiver (RX) band [2].

The present large scale use of fast electronic devices with possible off-band electromagnetic emissions has caused concerns in mobile telecommunications operators, whose mobile phone base station technology relies on stable and low RX band background noise level. The technology is based on the Wideband Code Division Multiple Access (W-CDMA) radio interface which is not particularly susceptible to coherent narrowband interference [3]. However, the received W-CDMA radio signal power levels are comparable to the background noise floor and, therefore, excessive noise level can partially or even totally prevent successful reception of uplink signals coming from mobile stations.

Background noise power level can be measured with sensitive microwave sensors. These devices are called microwave radiometers. A microwave radiometer passively measures the amount of electromagnetic energy arriving from the scene under observation through its antenna beam. Main applications of radiometric measurements fall under the title of remote sensing, which include atmospheric temperature retrieval, estimation of liquid water of clouds, soil moisture content and snow water content measurements, and so on. Microwave radiometry was first developed from the 1930s onwards to measure extraterrestial microwave radiation. In Teknillinen korkeakoulu (TKK), the Department of Radio Science and Engineering (formerly the Radio Laboratory and the Laboratory of Space Technology) has a long history in the development of radiometric theory and applications [4], [5], [6]

An L-band frequency scanning radiometer for monitoring the UMTS RX band background noise is developed and realised in this Licentiate thesis work. The theory on which the radiometer design is based is introduced in Chapter 2. In Chapter 3, the design of the L-band frequency scanning radiometer is documented. Verification of the design is carried out by laboratory tests and on-site measurements presented in Chapters 4 and 5, respectively. Finally, the work is summarised and the results of this thesis are discussed in Chapter 6.

2 Radiometry and radiometer systems

A radiometer measures electromagnetic radiation. Unlike communications or radar receivers which usually process phase-coherent signals, a radiometer is mainly used to measure phase-incoherent noiselike natural radiation extending the whole electromagnetic spectrum. Also, in traditional receivers the signal-to-noise ratio (SNR) needs to be as high as possible in order to successfully retrieve the signal information. The situation is quite different in a radiometer which measures radiometric signals that are often much smaller than the self-emitted noise power of the radiometer. [6]

This chapter first looks into the physical phenomena of thermal radiation and then establishes the relation between power received by an antenna and radiometric temperature, followed by determination of the fundamental design constraints of radiometers. Finally, the most widely used types of radiometer systems are introduced.

2.1 Brightness temperature

When electromagnetic radiation is incident on an object, a part of it is scattered and part of it is absorbed by the matter. The absorbed energy increases the thermal energy of the object, leading to increase in temperature. In a reverse process the object strives to remain in thermodynamic balance with its environment by emitting a part of the thermal energy as electromagnetic or "thermal" radiation.

In an atomic level, the absorption of a photon increases the quantum energy level of the particle by some finite amount, resulting in an absorption or emission line spectrum. When the number of particles is large, the corresponding increase in number of degrees of freedom leads to a continuous emission spectrum. Radiation by an atom is caused by collision with another particle and the probability of such an event increases as a function of the atom or particle's kinetic energy. Since kinetic energy of a particle is directly related to its thermal energy, the intensity of electromagnetic emission increases with temperature. [6]

2.1.1 Planck's blackbody radiation law

The relation between temperature of a blackbody and radiation intensity is defined by Planck's radiation law. A blackbody is defined as an ideal object which absorbs all incident radiation, reflecting none. In order to remain in thermal equilibrium, it also emits an equal amount energy. The radiation intensity of a blackbody is

$$B_f = \frac{2hf^3}{c^2}\left(\frac{1}{e^{hf/kT}-1}\right),$$
(2.1)

where B_f is the blackbody spectral brightness [Wm^{-2}sr^{-1}Hz^{-1}], h is Planck's constant, f is frequency, k is Boltzmann's constant, T is absolute temperature and c is velocity of light. Fig. 2.1 demonstrates the blackbody spectral brightness as a function of frequency at temperatures of 300 K, 1000 K and 10000 K. [6]

The low and high frequency parts of the Planck's radiation law can be approximated with the Rayleigh-Jeans law and the Wien radiation law, respectively. In the lower frequencies where $hf/kT << 1$, the exponent function $e^{hf/kT} - 1$ in Eq. (2.1) can be replaced by its approximation hf/kT. Substituting into Eq. (2.1), the Rayleigh-Jeans law is obtained as

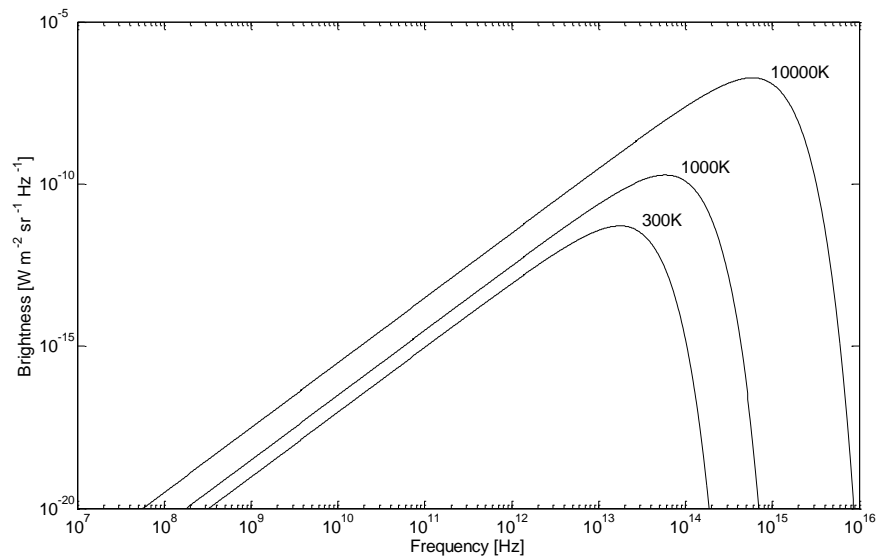$$B_f = \frac{2kT}{\lambda^2},$$
(2.2)

Figure 2.1. Blackbody spectral brightness at 300 K, 1000 K and 10000 K.

where λ is wavelength of the blackbody radiation. Planck's radiation law and Rayleigh-Jeans law for a blackbody at 300 K are shown in Fig. 2.2. The maximum error of Rayleigh-Jeans law at UMTS RX band is only 0.02 %, validating its use. [6]

2.1.2 Nonblackbody radiation

Real materials do not absorb all incident radiation as an ideal blackbody, but they do exhibit similar spectral brightness depence as that in Eq. (2.1). The spectral brightness of these gray bodies in thermal equilibrium is always less than for a blackbody in equal temperature. The total brightness B_{bb} [Wm^{-2}sr^{-1}] of a blackbody in a narrow bandwidth Δf at microwave frequencies is defined as

$$B_{bb} = B_f \Delta f = \frac{2kT}{\lambda^2} \Delta f .$$
(2.3)

For a homogeneous gray body at equal physical temperature, it is possible to define a blackbody equivalent brightness temperature. The brightness temperature $T_B(\theta,\varphi)$, which may be direction-dependent, allows the definition of the gray body brightness $B(\theta,\varphi)$ as

$$B(\theta,\varphi) = \frac{2k}{\lambda^2} T_B(\theta,\varphi) \Delta f .$$
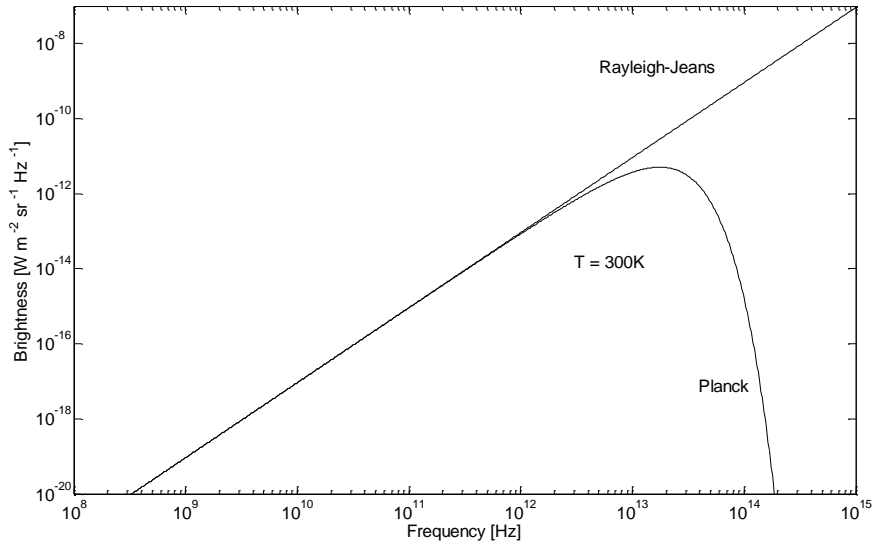(2.4)

Figure 2.2. Comparison of Planck's and Rayleigh-Jeans radiation laws for a blackbody at 300 K.

Emissivity $\varepsilon(\theta,\varphi)$, the ratio between the brightness of a real material and the brightness of a blackbody when both materials are in thermal equilibrium is

$$\varepsilon(\theta,\varphi) = \frac{B(\theta,\varphi)}{B_{bb}} = \frac{T_B(\theta,\varphi)}{T}.$$ (2.5)

Emissivity is always less than or equal to 1 and therefore the brightness temperature of a real object is cooler than its actual physical temperature. [6]

2.2 Antenna temperature

2.2.1 Power received by an antenna

When an antenna with an effective area A_r is observing a scene over solid angle Ω_t in the direction of maximum directivity, the received power can be shown to be

$$P = B_{mb}A_r\Omega_t,$$ (2.6)

where B_{mb} is brightness in the main beam direction. Removing the restriction of maximum directivity, the power received by an antenna over a finite bandwidth Δf is

$$P = \frac{1}{2}\int_f^{f+\Delta f}\iint\limits_{4\pi} B_f(\theta,\varphi)G_n(\theta,\varphi)d\Omega df,$$ (2.7)

where G_n is the normalised directivity of the antenna and the ½ factor arises from the fact that $B_f(\theta,\varphi)$ is unpolarised and the antenna is polarised. [6]

2.2.2 Power-temperature relation

Power-temperature relation can be studied by placing a lossless antenna inside a blackbody chamber at constant temperature T and observing the output power at the antenna terminals. Over a narrow bandwidth where the spectral brightness B_f is approximately constant, the available power is found by inserting Eq. (2.2) into Eq. (2.7) and integrating over frequency:

$$P_{bb} = kT\Delta f \frac{A_r}{\lambda^2}\iint\limits_{4\pi} G_n(\theta,\varphi)d\Omega,$$ (2.8)

Since the integral in Eq. (2.8) is equal to the pattern solid angle Ω_p and Ω_p is related to antenna effective aperture by $\Omega_p = \lambda^2/A_r$, Eq. (2.8) reduces to

$$P_{bb} = kT\Delta f \; . \tag{2.9}$$

Eq. (2.9) establishes a linear relationship between power and temperature. It is also analogous to the available noise power of a resistor at temperature T over bandwidth Δf, a convenient fact that facilitates radiometer calibration. [6]

2.2.3 Efficiency and antenna temperature

Fig. 2.3 shows a typical measurement situation where the antenna delivers an output power proportional to the apparent temperature distribution $T_{AP}(\theta,\varphi)$. $T_{AP}(\theta,\varphi)$ is a blackbody-equivalent temperature distribution, which corresponds to the sum of brightness temperatures representing to the incident electromagnetic energy. Antenna radiometric temperature T_A is defined as a resistor-equivalent power at the radiometer input resulting from the apparent temperature distribution as

$$P = kT_A\Delta f \; . \tag{2.10}$$

Antenna temperature contains components arriving from main beam and side lobe directions. The specific objective in microwave remote sensing is to relate the brightness temperature in the main beam solid angle to the radiometer output voltage V_{out}, which requires knowledge on side lobe level relative to the main beam and on the apparent temperature distribution in the sidelobe direction. For the purposes of observing the background noise level in UMTS RX band, the distinction between the
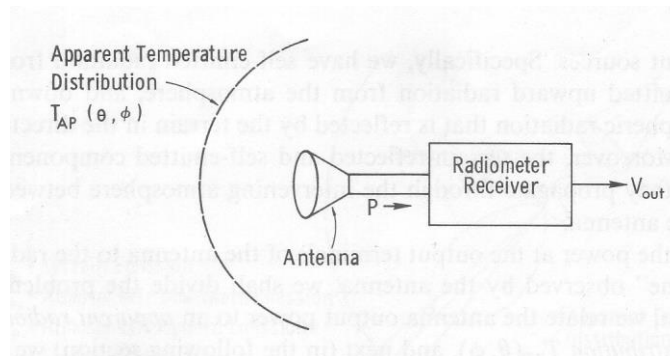

Figure 2.3. Power receiver by antenna is proportional to the surrounding apparent temperature distribution [6].

above mentioned components is not relevant.

So far, an ideal antenna has been considered. A part of the incident radiation is absorbed as heat in a practical antenna. Antenna radiation efficiency η_l is defined as the ratio of the received power to the incident power. A lossy antenna is also a source of radiation itself, corresponding to an output noise temperature T_N

$$T_N = (1 - \eta_l)T_{phys}, \tag{2.11}$$

where T_{phys} is the physical temperature. The antenna temperature of a lossy antenna $T_A^{'}$ is therefore [6]

$$T_A^{'} = \eta_l T_A + (1 - \eta_l)T_{phys}. \tag{2.12}$$

2.3 Device noise characterisation

The purpose of a radiometer is to detect the antenna temperature, which is a fluctuating noise-like signal. It is therefore only possible to measure an estimate of the antenna temperature. The precision to which the measurement can be performed determines the radiometer measurement uncertainty ΔT. ΔT is defined to be equal to the standard deviation of a zero-mean Gaussian probability distribution. [6]

As mentioned earlier, the measurement of radiometric temperature is analogous to the measurement of power delivered by a resistor at temperature T to a matched load through an ideal rectangular filter of bandwidth B. The thermal noise of the resistor is zero mean and has a non-zero root-mean-square (RMS) value. The concept of resistor-equivalent noise temperature can also be used in the description of any band-limited noise source. This facilitates the noise characterisation of a radiometer system, which includes many kinds of active and passive devices. [6]

2.3.1 Input noise temperature

The concept of effective input noise temperature T_E is used in the analysis of output noise power of a general linear two-port device. Effective input noise temperature is defined to be the temperature of a resistor which, if placed at input of an ideal noise-free

device, generates an equal amount of noise power at the device output as a non-ideal noisy device. The noise power P_{no} at the output is

$$P_{no} = GkT_{E}B,$$

(2.13)

where G is the gain of the device and B is the noise bandwidth. In the presence of actual input noise temperature T_N, the total output noise power is

$$P_{no} = Gk(T_N + T_E)B.$$

(2.14)

The noise temperature of a general lossy device (i.e. an attenuator), defined by a loss factor L, is

$$T_E = (L-1)T_{phys}.$$

(2.15)

In case of conventional receivers, the noise performance is usually described by the alternative concept of noise factor F. Noise factor is a measure of the degradation of signal-to-noise ratio between device input and output ports of the device. The relation between effective input noise temperature and noise factor is

$$F = \frac{T_E}{T_0} + 1,$$

(2.16)

where the physical temperature T_0 is standardised to 290 K. [6]

2.3.2 Noise temperature of a cascaded system

A radiometer contains an N number of noisy devices. The concept of effective input noise temperature is now extended to a cascaded system. Provided that the individual devices are impedance matched, the overall effective input noise temperature T_E is

$$T_E = T_{E1} + \frac{T_{E2}}{G_1} + \frac{T_{E3}}{G_1 G_2} + \cdots + \frac{T_{EN}}{G_1 G_2 \cdots G_{N-1}},$$

(2.17)

where T_{EN} and G_N are the effective input noise temperature and gain of the Nth stage, respectively. It is apparent from Eq. (2.17), that the gain and input noise temperature of the first stage of the cascaded system largely determines the total input noise temperature. [6]

2.3.3 Radiometer noise temperature

Fig. 2.4 demonstrates the practical situation for a radiometer with an (input) noise temperature of T_{REC}. Most often the antenna cannot be directly attached to the radiometer input, it is instead connected via a lossy transmission line. Applying Eq. (2.17), the effective input noise temperature T'_{REC} of the transmission line - receiver cascade is

$$T'_{REC} = (L-1)T_{phys} + LT_{REC}.$$
(2.18)

It is now possible to establish the total output noise power of a radiometer system P_{SYS} in terms of the effective input noise temperature at the antenna terminals in Fig. 2.4 by combining Eqs. (2.12), (2.15) and (2.18) as

$$P_{SYS} = Gk(T'_A + T'_{REC})B = Gk[\eta_l T_A + (1-\eta_l)T_{phys} + (L-1)T_{phys} + LT_{REC}]B,$$
(2.19)

where G is the radiometer overall gain. For a superheterodyne radiometer, bandwidth B is typically governed by the intermediate frequency (IF) section. From Eq. (2.19), the effective system input noise temperature T_{SYS} is

$$T_{SYS} = \eta_l T_A + (1-\eta_l)T_{phys} + (L-1)T_{phys} + LT_{REC}.$$
(2.20)

2.4 Radiometer systems

The purpose of a radiometer is to measure T_A in Eq. (2.20) with a high degree of accuracy. The actual output power is proportional to T_{SYS}, G and B according to Eq. (2.19). T_A is then calculated from Eq. (2.20), provided that η_l, L and T_{phys} are known.
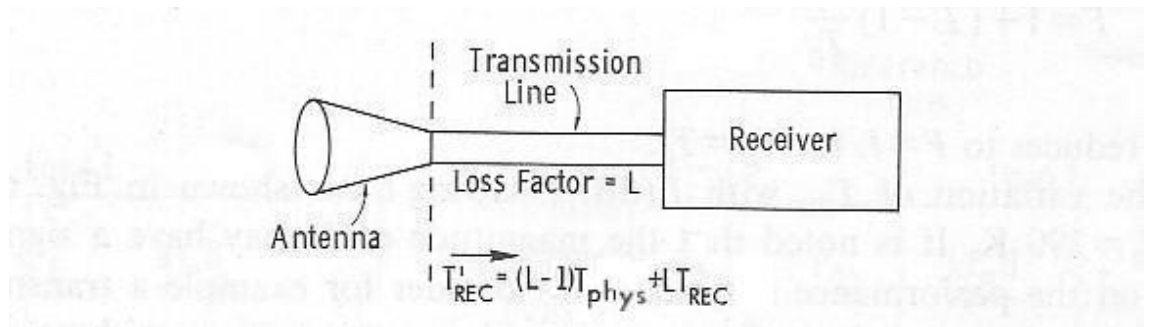

Figure 2.4. Effective input noise temperature of an equivalent transmission line - noise-free receiver cascade [6].

The radiometer is calibrated by replacing the antenna with a noise source having a known input noise temperature and monitoring the corresponding output power. Radiometers typically use square-law detection, in which case the detector output voltage is linearly related to the input noise temperature.

Radiometer measurement performance is determined by two fundamental attributes: measurement accuracy and sensitivity. Measurement sensitivity ΔT is equal to the smallest perceptible chance in antenna temperature. It depends on radiometer bandwidth B, integration time τ and system equivalent input noise temperature T_{SYS} as

$$\Delta T = C \frac{T_{SYS}}{\sqrt{B\tau}} , \qquad\qquad (2.21)$$

where C is a constant number (1 or more) depending on the radiometer type [4]. Measurement accuracy is defined to be the difference between the actual antenna temperature and the measurement result. Main contributors to measurement accuracy are calibration precision and specifically the accuracy in which the calibration load noise temperatures are known and drifts in gain or radiometer noise temperature. [6]

2.4.1 Total power radiometer

Fig. 2.5 depicts a simple kind of system, called the total power radiometer. It consists of an antenna, a predection section that processes the input noise signal to be suitable for detection in the square-law detector and finally a low-pass filter. In a double-sideband receiver configuration, two RF bands of width B centered around the
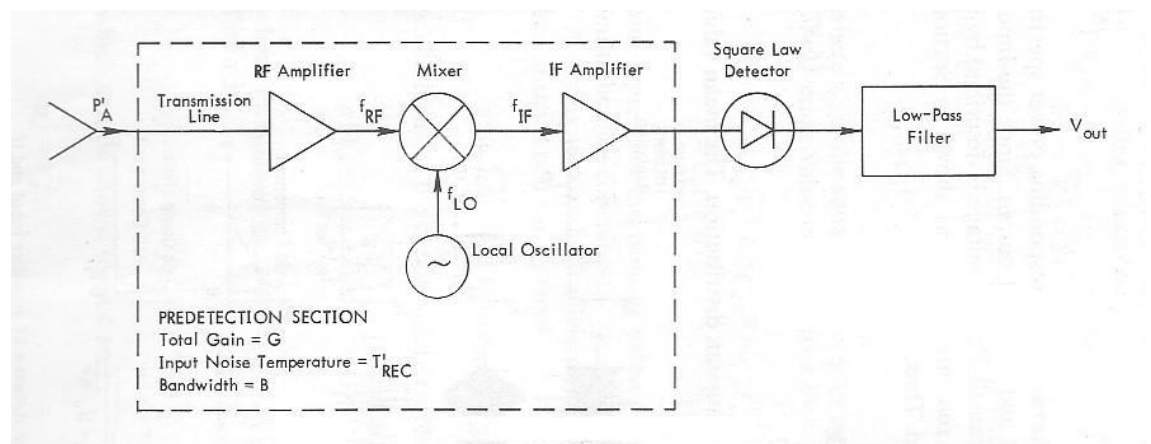

Figure 2.5. Block diagram of a total power radiometer [6].

frequencies $f_{RF} = f_{LO} \pm f_{IF}$ are translated to the intermediate frequency f_{IF} and amplified. In radiometric measurements a single-sideband topology is usually used, where one the RF bands is amplified by the RF amplifier and the other band is rejected. The RF-amplifier bandwidth B_{RF} is often wider than the IF-amplifier bandwidth B, it is therefore the latter which determines the predection section bandwidth. After detection, the low-pass filter is then used to filter out the high frequency components from the detector output voltage V_d. Filtering in frequency domain is equivalent to averaging voltage V_d in the time-domain over a time interval τ. The resulting radiometer DC output voltage $\overline{V}_{out}$ is

$$\overline{V}_{out} = g_{LF} C_d G k T_{SYS} B \,, \tag{2.22}$$

where g_{LF} is the low-pass filter gain and C_d is the detector power-sensitivity constant. [6]

The total noise radiometer is simple to construct and use. Its sensitivity is

$$\Delta T = \frac{T_{SYS}}{\sqrt{B\tau}} = \frac{T_A^{'} + T_{REC}^{'}}{\sqrt{B\tau}} \,. \tag{2.23}$$

Successful operation, however, requires that output voltage fluctuations due to gain variation are much smaller than the variation due to antenna temperature. Low frequency gain variations can be effectively filtered by calibrating the radiometer as regularly as needed. Fast radiometer gain fluctuations ΔG are harder to avoid and cause an rms uncertainty of

$$\Delta T_G = T_{SYS} \left(\frac{\Delta G}{G} \right). \tag{2.24}$$

Gain variations can be partly suppressed by maintaining the radiometer at a stable physical temperature and regulating the amplifier power supplies. The measurement uncertainties due to the measurement of a noise-like signal and due to gain variations can be considered uncorrelated. Combining Eqs. (2.23) - (2.24), the total power radiometer overall measurement uncertainty (sensitivity) is [6]

$$\Delta T = T_{SYS} \left[\frac{1}{B\tau} + \left(\frac{\Delta G}{G} \right)^2 \right]^{\frac{1}{2}}.$$ (2.25)

2.4.2 Dicke radiometer

Dicke radiometer uses modulation in order to diminish the effect of gain fluctuations and variations in radiometer noise temperature. Fig. 2.6 shows a simplified block diagram of a Dicke radiometer, where the input is switched periodically between the antenna and a stable reference load. The detector output voltage is multiplied with either plus or minus one in syncronism with the input switch and then integrated over time. The measurement result is therefore only dependent on the difference between $T_A^{'}$ and T_{REF} and independent on the radiometer noise temperature T_{REC}. Modulation frequency f_S has to be greater than the highest significant component of the gain fluctuation spectrum. Most of the gain variations occur at frequencies below 1 Hz and have neglible components above 1 kHz. The total measurement uncertainty of a Dicke radiometer is

$$\Delta T = \left[\frac{2 \left(T_A^{'} + T_{REC}^{'} \right)^2 + 2 \left(T_{REF} + T_{REC}^{'} \right)^2}{B\tau} + \left(\frac{\Delta G}{G} \right)^2 \left(T_A^{'} - T_{REF} \right)^2 \right]^{\frac{1}{2}}.$$ (2.26)

If the radiometer is balanced, in which case $T_A^{'}$ is chosen to be equal to the average antenna temperature resulting from the observed apparent temperature distribution, Eq. (2.26) reduces to

$$\Delta T \approx \frac{2 \left(T_A^{'} + T_{REC}^{'} \right)}{\sqrt{B\tau}}.$$ (2.27)

The factor 2 in Eq. (2.27) arises from the fact that only half of the integration time is spent measuring the antenna temperature. Sensitivity can be improved by modifying the modulating signal pulse ratio in order to increase the time interval in which the antenna signal is measured. [6], [7]
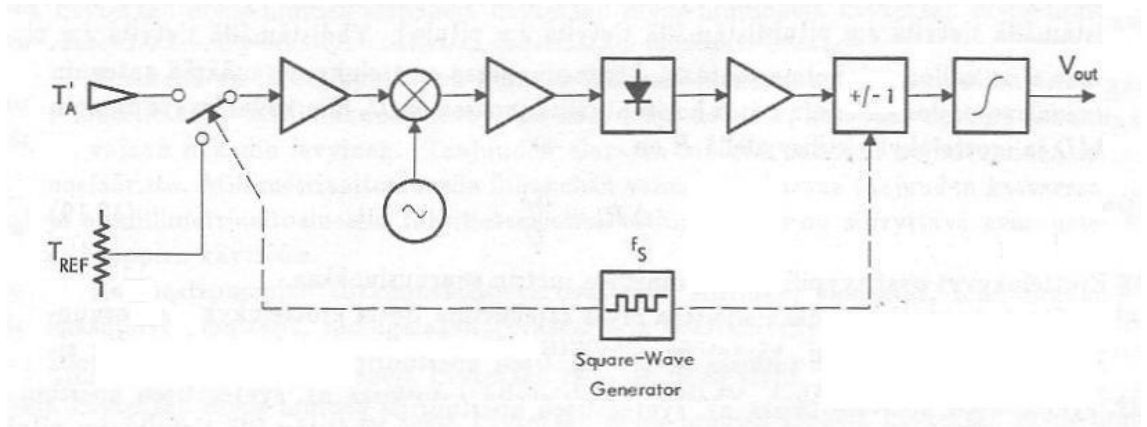
Figure 2.6. Block diagram of a Dicke radiometer [6], [7].

2.4.3 Noise-injection radiometer

Noise-injection radiometer (in Fig. 2.7) improves upon the Dicke radiometer by maintaining the antenna temperature continuously equal to the reference load temperature. A variable noise source is used to feed a servo loop controlled amount of excess noise to the signal path during the interval in which the antenna temperature is measured. Fulfilling the balanced condition $T_A^{'} = T_{REF}$ at all times virtually eliminates the measurement uncertainties due to radiometer noise temperature and gain fluctuations. Measurement uncertainty of a noise-injection radiometer is [8]

$$\Delta T = \frac{2\left(T_{REF} + T_{REC}^{'}\right)}{\sqrt{B\tau}}. \tag{2.28}$$
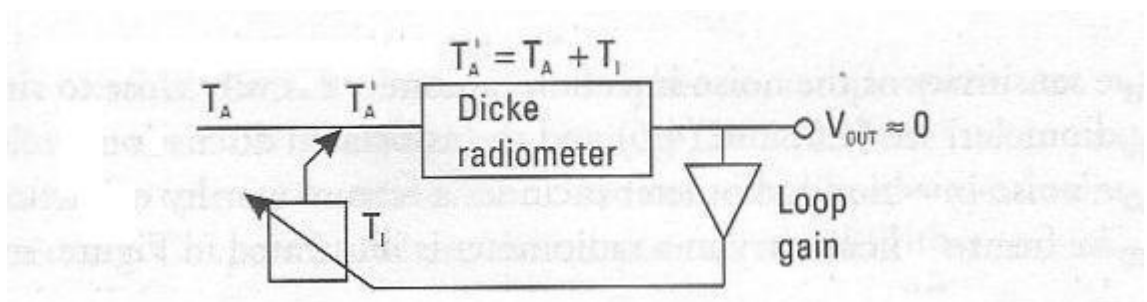
Figure 2.7. Block diagram of a noise-injection radiometer. $T_A^{'}$ is kept equal to the reference load noise temperature by injecting excess noise temperature T_I during antenna temperature measurement period [9].

3 Design of the L-band frequency scanning radiometer

The design and realisation of L-band frequency scanning radiometer is a part of L-band Interference Measurements in Urban and Suburban Environment (LIME) project, funded by TKK, Nokia Siemens Networks Oy (NSN) and the Finnish Funding Agency for Technology and Innovation (Tekes) [10]. The LIME project is related to the work done at TKK in the European Space Agency's (ESA) Soil Moisture and Ocean Salinity (SMOS) mission [11]. Within the framework of the SMOS mission, an airborne L-band 2-D interferometric radiometer HUT-2D was developed at the TKK's Laboratory of Space Science [5], [12]. As a preliminary study in LIME, the HUT-2D instrument was used to measure man-made radio interference in the greater Helsinki area within the protected part of the L-band (1.4 – 1.427 GHz), which is reserved for radio astronomy.

A further two L-band instruments for monitoring the L-band are envisaged in the LIME project, second of which is the frequency scanning radiometer (FIRaL). The design of the FIRaL instrument is based on the technology of the HUT-2D radiometer and the other LIME project instrument, the 1.4 GHz radiometer (aL-Band). For background information, relevant parts of the previous two are presented in this Chapter. The system requirements and specification of the FIRaL instrument are defined next, followed by the design of individual system components.

3.1 Recent radiometer development at TKK

3.1.1 HUT-2D interferometric radiometer

The HUT-2D instrument is an interferometric radiometer, which uses aperture synthesis for image construction. It has 36 L-band microwave receivers, each measuring the same target with integrated dual-polarised microstrip patch antennas and providing in-phase (I) and quadrature phase (Q) IF outputs. The receivers are in an U-shaped 2 m x 2 m configuration, as shown in Fig. 3.1. The receivers are based on the superheterodyne total power radiometer principle, as described in Section 2.4.1. Receiver amplitude calibration is performed by an accurately characterised central noise source (CNS) having two output power levels of warm and hot. The CNS unit is temperature
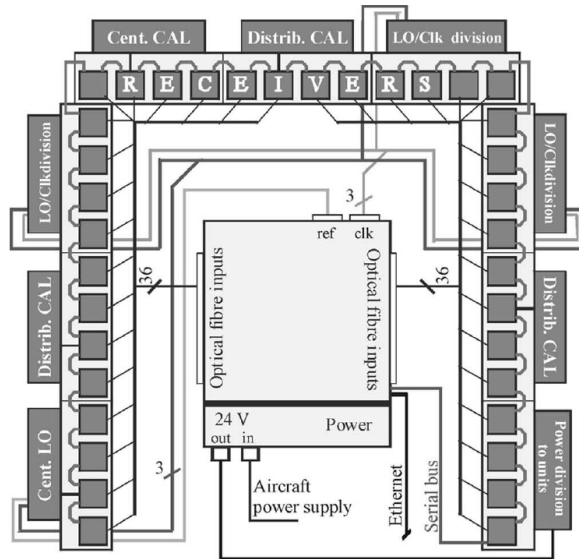
Figure 3.1. HUT-2D instrument layout showing subsystem locations [5].

stabilised with heating elements and associated control electronics. The CNS signals are coupled to the receiver input via a single-pole 4-throw switch in the receiver input (Fig. 3.2). The switch is also used to select either antenna polarisation or a passive calibration load at the receiver physical temperature. It is worth pointing out that the placement of the RF filter after the RF amplifier in Fig. 3.2 is a compromise, the aim of which is to minimise the radiometer noise temperature. It does, however, leave the receiver susceptible to possible compression effects due to strong off-band interference signals in the RF amplifier bandwidth. [5]

Other major components of the instrument are the local oscillator subsystem, which provides the LO signal for all 36 receivers, a digital correlator for image construction,
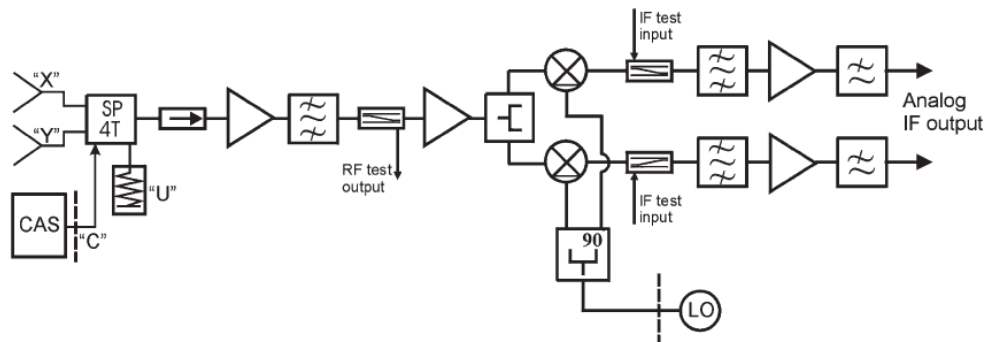

Figure 3.2. Block diagram of one of the HUT-2D receivers [5].

power supply, operating computer and receiver control boards (RCBs). The 36 RCBs are responsible for IF signal sampling, collecting the physical temperature data of receivers via sensors and transmission of control signals and supply power to receivers, local oscillator and calibration subsystems. [5]

3.1.2 aL-Band radiometer

The aL-Band total power radiometer is an enhanced version of a single HUT-2D instrument receiver. It features a redesigned RF front-end connected to the HUT-2D receiver. The two main objectives are to achieve greater radiometric sensitivity by placing the portable RF front-end in the direct vicinity of the used L-band horn antenna and obtaining better stability by maintaining the unit in constant temperature with controlled heating elements. The heating is realised with transistor driven resistors on a thin printed circuit board (PCB), which is placed on the bottom side of a 2 mm aluminium plate, the top of which houses the RF front-end PCB. Temperature control is governed by thermal control board (TCB) electronics. The design is an adaptation of the HUT-2D CNS unit temperature stabilisation. [13]

The RF front-end in Fig. 3.3 houses an active cold load (ACL) [14] for calibration purposes. The ACL is based on a reversely connected low-noise amplifier. The equivalent available noise temperature in the amplifier input is less than the physical temperature of the amplifier. The realised ACL resistor-equivalent noise temperature is
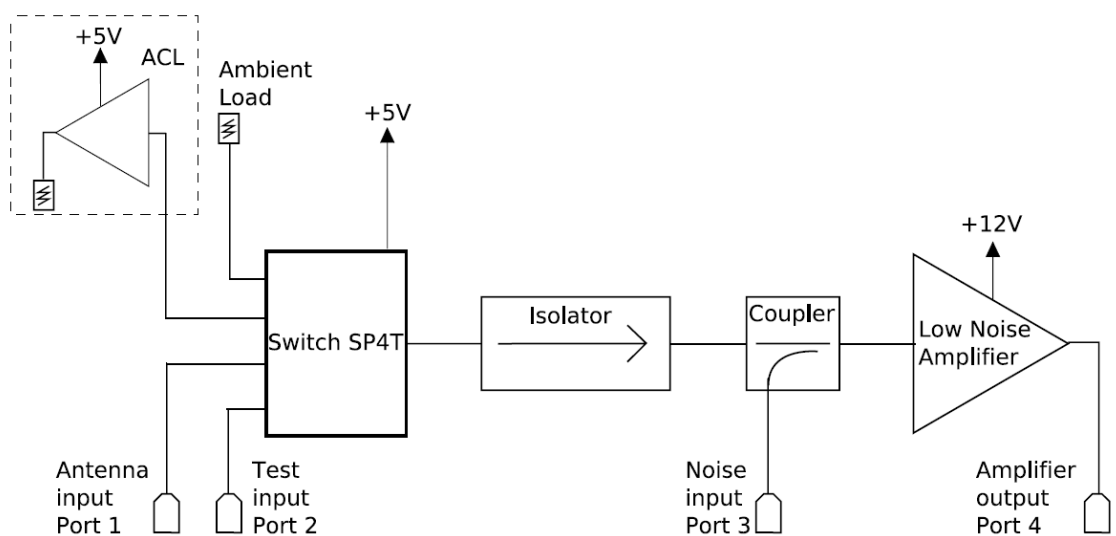

Figure 3.3 aL-Band RF front-end block diagram [13].

measured to be around 170 K. The aL-Band radiometer is yet to be fully realised. [13]

3.2 System specifications and design outlines

The FIRaL is a single channel receiver and is based on the total power radiometer principle, which is also used in HUT-2D and aL-Band instruments. The center frequency is 1950 MHz instead of 1.4 GHz, necessitating a complete redesign of the LO, RF and IF subsystems. The block diagram level design of the new radiometer is based on the design of the earlier radiometers. IF sampling and data acquisition will be done using a RCB identical to that used in each HUT-2D receiver. Temperature control of the RF and IF electronics is realised with a heater board and TCB, similarly as with the aL-Band RF front-end. A pyramidal horn antenna for scene observation is designed and personal computer (PC) control software is developed. Additionally, an enclosure for housing the subsystems is procured and modified.

System requirements are mainly defined by the LIME project corporate partner NSN. The instrument must be able to measure background noise levels between $0 - 1000$ K with a sensitivity of 10 K or better. The required 3-dB field-of-view for the horn antenna is 30° in both E- and H-planes. The receiver has to be able to measure the UMTS RX band (1920-1980 MHz) in 1 MHz steps, while having 5 MHz 3-dB bandwidth. The radiometer should be small and portable, facilitating measurements in demanding locations, such as link masts and roof tops. NSN has provided the specific operating band RF front-end components and the requirement is to achieve the best possible design with these and other available resources while meeting the specifications.

3.2.1 FIRaL system level design

FIRaL system level block diagram is illustrated in Fig. 3.4. The system has three main physical entities of horn antenna, radiometer main box and control computer. The main box houses four separate electromagnetically shielded enclosures for the receiver, LO, RCB and TCB printed circuit boards. RCB also has an integrated temperature control for the temperature sensitive detector diodes, which perform the square law detection. Each of the four subenclosures of the main box have dimensions of 147 mm x 147 mm x 25 mm or smaller, leading to a relatively compact main enclosure size.
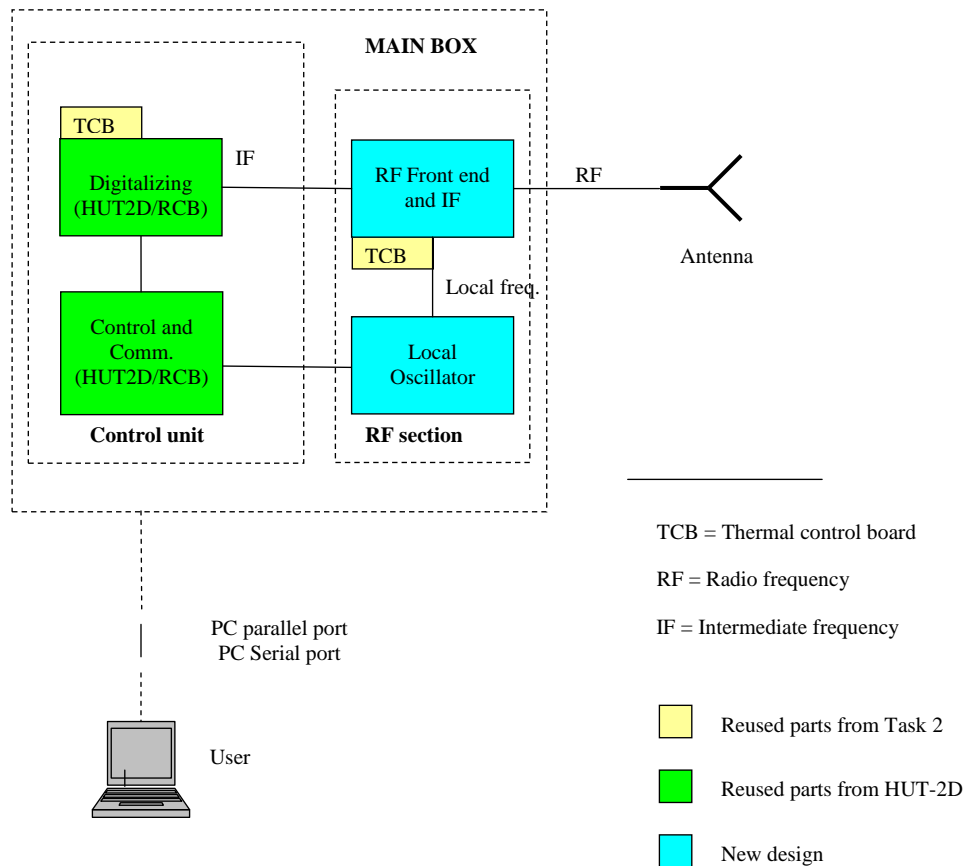
Figure 3.4. FIRaL system configuration. Elements of the main box which are identical to those in Task 2, are marked yellow, while elements from HUT-2D instrument are in green. LO and RF front-end are new designs [10].

The receiver PCB houses the single sideband superheterodyne total power radiometer RF amplifier, mixer and IF amplifier stages, including an input switch with two antenna inputs (only one is used), an input for "hot" ambient temperature calibration load and an input for "cold" active calibration load. IF of 70 MHz is chosen, for which the LO board provides a programmable LO signal between 1990-2050 MHz, depending on the desired RF band. Communication between the control computer and the RCB, LO and TCB subsystems is realised through a single PC parallel port and a single PC serial port. Development of control software is outsourced to an outside contractor. The control computer runs on regular line current and the main box requires 18-36 V (28 V nominal) DC power. RCB provides regulated DC power to the receiver and LO boards. Fig. 3.5 shows the connections between subsystems.
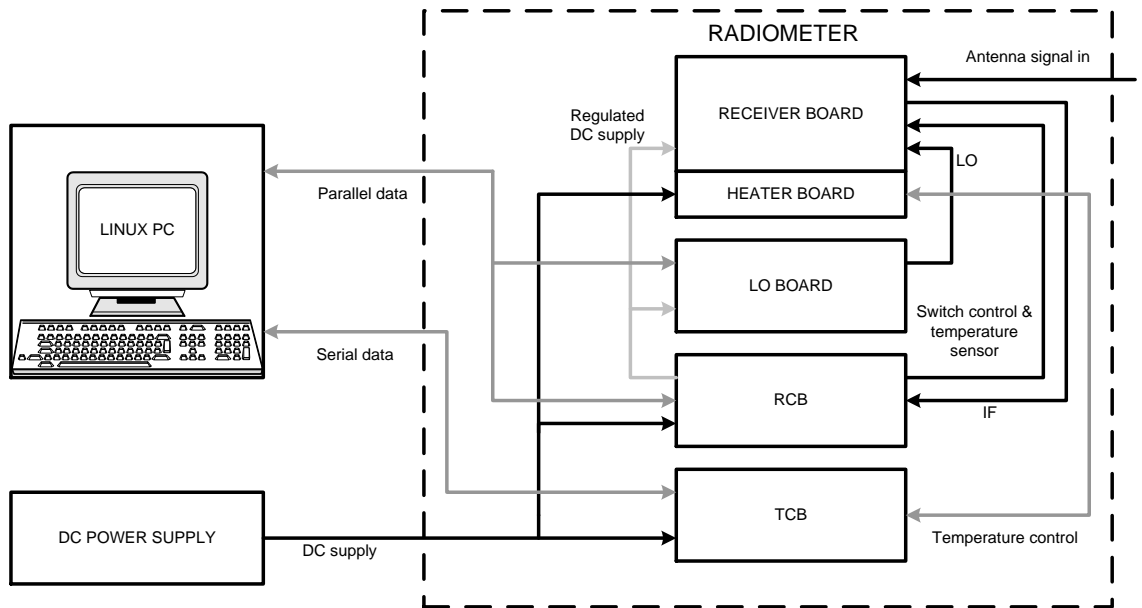
Figure 3.5. FIRaL radiometer system wiring. Antenna is omitted.

Detailed descriptions of the receiver board, LO board and antenna subsystem designs are discussed in the following Sections. RCB and TCB units, along with the receiver board temperature stabilisation design are reused from the previously developed radiometers and will not be further elaborated here.

3.2.2 Electronic design flow

The schematic and PCB designs are implemented with PADS Logic and PADS Layout software by Mentor Graphics, respectively [15]. Circuit operation near 2 GHz requires proper RF design techniques and microstrip transmission lines with controlled impedance levels are used in this work. Fundamental microstrip transmission line theory is widely presented in literature and will not be repeated here [16], [17]. In order to facilitate the design process, numerical computing software MATLAB by The MathWorks [18] and electronic design software Advanced Design System (ADS) by Agilent are used [19].

RF design essentially requires that transmission line impedances are known and that any ports which are not equal to the transmission line characteristic impedance are matched. Impedance matching can be realised with parallel tuning stubs, serial waveguide elements, such as a quarter-wave transformer or a tapered section, or with lumped components [16]. The latter technique is used in the FIRaL instrument receiver and LO boards in order to keep the circuit layout compact.

30

Impedance matching with lumped components can be realised with two possible ways, illustrated in Fig. 3.6. Z_o is the transmission line characteristic impedance, $Z_L = R_L + jX_L$ is the load impedance, while jX and jB are the serial and parallel matching element impedances, respectively. If $R_L < Z_L$, the circuit of Fig. 3.6 (a) should be used, otherwise the circuit of Fig. 3.6 (b) should be used.

If the circuit of Fig. 3.6 (a) is used, the reactance X and susceptance B are

$$X = \pm\sqrt{R_L(Z_0 - R_L)} - X_L \tag{3.1}$$

$$B = \pm\frac{\sqrt{(Z_0 - R_L)/R_L}}{Z_0}. \tag{3.2}$$

There are two possible solutions for matching elements, as seen in Eqs. (3.1) and (3.2). A positive X or a negative B implies an inductor, while a negative X or a positive B implies a capacitor. In the case of circuit of Fig. 3.6 (b), the element values are

$$B = \frac{X_L \pm \sqrt{R_L/Z_0}\sqrt{R_L^2 + X_L^2 - Z_0 R_L}}{R_L^2 + X_L^2} \tag{3.3}$$

$$X = \frac{1}{B} + \frac{X_L Z_0}{R_L} - \frac{Z_0}{BR_L}, \tag{3.4}$$

again with two possible solutions. The normalised reactance $x = X/Z_0$ corresponds to an inductance L of
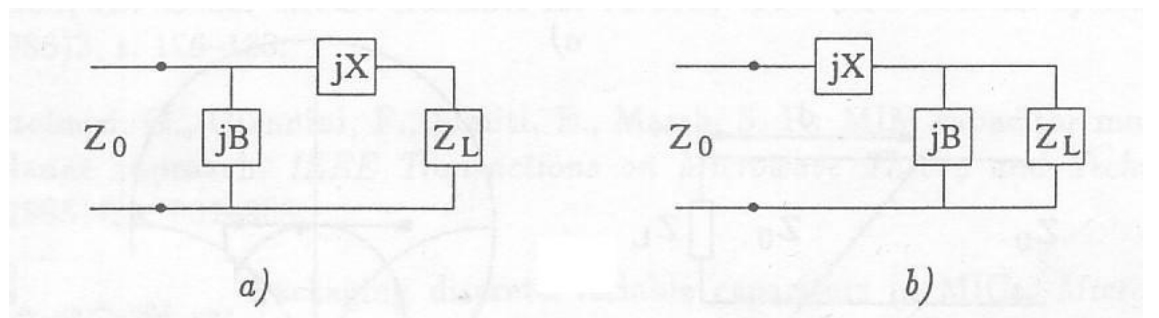
$$L = xZ_0/\omega, \tag{3.5}$$

Figure 3.6. Impedance matching with lumped components [16].

or a capacitance C of

$$C = -1/(xZ_0\omega), \tag{3.6}$$

where ω is angular frequency. Similarly, the normalised susceptance $b = BZ_0$ corresponds to a capacitance of

$$C = b/(Z_0\omega), \tag{3.7}$$

or an inductance of [7], [16], [17]

$$L = -Z_0/(b\omega). \tag{3.8}$$

The circuit design process starts with a high level block diagram presentation. Individual circuit schematic blocks are then designed in PADS Logic around the main component, e.g., an amplifier, based on datasheet recommendations, while observing general guidelines on proper shielding, power supply decoupling and grounding [20]. Eqs. (3.1) – (3.8) are solved in MATLAB in order to find an ideal matching network for any component ports requiring impedance matching. The actual physical realisation of the circuit is then simulated and optimised at the frequency of operation in ADS, based on the ideal matching network elements and datasheet guidelines. Finally, the circuit block layout is drawn in PADS layout, from which the software files for PCB manufacturing can be produced.

3.3 Receiver board design

The inputs for receiver design are determined by the specified sensitivity requirement and RCB detector block square-law detector response. The IF output power level from the receiver PCB must be in the square-law part of the detector diode operating curve, while being at a suitable level for successful analog-to-digital conversion (ADC). The HUT-2D instrument receiver gains are between 90 to 93 dB [5]. Again for the HUT-2D receiver, assuming a total system input noise temperature of 700 K and an IF filter bandwidth of 7 MHz [5], the resulting output power is from -12 to -9 dBm, according to Eq. (2.14). From previous experience, it is noted that the optimum input power for the RCB square-law detector is around 10 dB less than the output power of a single HUT-

2D receiver. Since the HUT-2D instrument RCB is also used in the FIRaL, an output power level of -20 dBm is used for gain calculations.

Radiometer input power level can be estimated by selecting for example an effective input noise temperature of 700 K and an effective antenna temperature of 300 K. Recalling that the IF filter bandwidth is 5 MHz, the input noise power is

$$P_{in} = k\left(T_A^{'} + T_{REC}^{'}\right)B = -101.6 \text{ dBm.} \tag{3.9}$$

The resulting optimum FIRaL receiver gain is around 82 dB, with any value between 80 to 90 dB being acceptable. With the above noise temperatures and an integration time of 250 ms, the measurement sensitivity due to a noise-like measurement signal is 0.9 K (Eq. (2.23)). The sensitivity requirement of $\Delta T \leq 10$ K is easily fulfilled and allows a wide margin for gain related measurement uncertainties.

3.3.1 FIRaL receiver board block diagram level design

The block diagram of the FIRaL receiver is shown in Fig. 3.7. The input switch with antenna input, hot and cold internal calibration loads form the first functional block. RF filter with three separate amplifier stages follows the input switch. The next functional block is the mixer stage. With the signal mixed to IF, the final functional block consists of a 5 MHz band-pass filter, two amplifier stages and a post band-pass filter in order to suppress any IF amplifier spurious signals. The design allows flexible switching between calibration loads and antenna feed with a 2-bit transistor-transistor logic (TTL) level control signal, provides enough gain for successful detection and translates the measured signal to 70 MHz IF, while rejecting the mixer mirror frequency (2060-2120 MHz).

The receiver is integrated on a 1.27 mm thick, 147 mm x 147 mm Rogers RT/Duroid 6010 LM PCB material using microstrip technology [21]. Surface mount devices (SMDs) are used throughout, facilitating component layout and leaving the whole PCB bottomside as a ground layer. The functional blocks in Fig. 3.7 are based on commercially available components. Starting from the input, the used components are: Hittite HMC241QS16 non-reflective switch [22], UBE Industries MD441 band pass filter for UMTS [23], Richardson Electronics RLAS1722A LNA [24], Maxim, Inc. MAX2641 LNA (two RF amplifiers and ACL) [25], Maxim, Inc. MAX2681
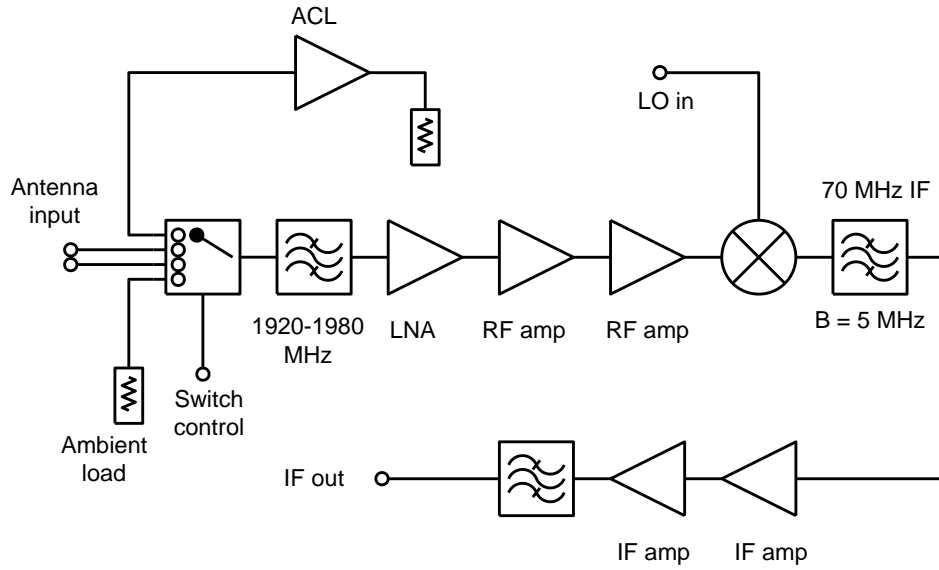
Figure 3.7. High-level FIRaL receiver block diagram.

downconverter mixer [26], Golledge Electronics MA08181 surface acoustic wave (SAW) filter [27], Maxim, Inc. MAX2650 IF amplifier [28], and Mini-Circuits ERA-3+ IF amplifier [29]. The final filter is realised with standard passive SMD inductors and capacitors.

The nominal gain and insertion loss values for the FIRaL receiver components in an impedance matched configuration are listed in Table 3.1. The second IF filter insertion loss is estimated to be 3 dB. The theoretical gain of the receiver is 92.4 dB, when all components are optimally matched. The desired gain is somewhat lower and therefore the outputs of the two RF amplifiers are left unmatched in order to arrive at an estimated gain value of 10 dB per amplifier, which in turn leads to a suitable estimated receiver total gain of 83.6 dB. Component noise figures *(10·log(F))* are also listed in Table 3.1. Typical values for active components are collected from device datasheets. The noise figures of lossy components are estimated by considering them purely resistive and calculated according to Eqs. (2.15) − (2.16), while noting that T_{phys} is chosen to be equal to T_0. However, in case of filters this assumption may not be valid.

The receiver input noise temperature can be solved by applying Eq. (2.17). The noise figures in Table 3.1 must first be converted to input noise temperatures by arranging Eq. (2.16) into

$$T_E = T_0(F - 1). \tag{3.11}$$

Table 3.1 FIRaL receiver gain

Component	Nominal gain	Designed gain	Noise figure	Reference
	dB	dB	dB	
Input switch	-0.5	-0.5	0.5	[22]
RF filter	-1.0	-1.0	1.0	[23]
LNA	30	30	0.55	[24]
RF amp	14.4	10	1.3	[25]
RF amp	14.4	10	1.3	[25]
Mixer	8.4	8.4	11.1	[26]
SAW filter	-8	-8	8	[27]
IF amp	19	19	3.9	[28]
IF amp	18.7	18.7	2.7	[29]
Band-pass filter	-3	-3	3	
Total gain	**92.4**	**83.6**		

The theoretical receiver input noise temperature is then $T_{REC} = 175.2$ K. The preceding result is much less than the 700 K noise temperature, which was used earlier and provides a solid basis for further receiver design and fulfills the sensitivity requirement. The use of Eq. (2.17) for calculating the input noise temperature of a cascaded system is valid when an approximate magnitude of the input noise temperature is studied, eventhough the condition of perfect impedance matching is not fulfilled. Ignoring the RF amplifier output impedance mismatch leads to negligible error in the calculated T_{REC} value, because the receiver input noise temperature is mainly determined by the input switch, RF filter and LNA. The input noise temperature of such a cascade is 174.9 K (Eq. (2.17)), which is nearly equal to the T_{REC} value of 175.2 K. A somewhat larger error occurs when the RF filter input return loss of 18 dB is ignored. Taking account the impedance mismatch of the filter result in a RF filter input noise temperature of 69.3 K, compared to the 75.1 K value which is obtained when the impedance mismatch is ignored. The receiver input noise temperature is similarly diminished to 168.6 K instead of 175.2 K.

3.3.2 Input switch design

In the receiver design, 50 Ω transmission lines are used throughout. For the Rogers PCB material of 1.27 mm height and an 10.2 effective electrical permittivity, the transmission line width is 1.161 mm at 1.95 GHz, while one wavelength is 58.962 mm. Figure 3.8 shows the input switch with the accompanying electronics. The switch has 4 input ports, an output port, two inputs for control, power supply pin, and 8 ground pins. Two SMA type cable connectors accept inputs to ports 1 and 2. Only one antenna input is used and the second cable connector is terminated with a matched load. Port 4 is connected to a 50 Ω SMD resistor, which acts as a hot calibration load. The active cold calibration load is attached to port 3. Power supply pins of both the ACL amplifier and input switch are connected to the receiver board +5V supply and decoupled with 330 pF capacitors. DC blocking capacitors are also placed in the switch input and output transmission lines.

The ACL design was initially based on a reverse connected conjugately matched two-port network. In conjugate matching both the input and output ports of the two-port network are conjugately matched, refer to [16] or [17] for design equations. During preliminary tests it was, however, noted that the response of the actual realised circuit differed greatly from the simulated response when conjugate matching for both the input and output ports was attempted. Small deviations of the actual component S-parameter values from the quoted manufacturer data are suspected [30], [31], with the resulting overall effect leading to unpredictable circuit behaviour. The practical
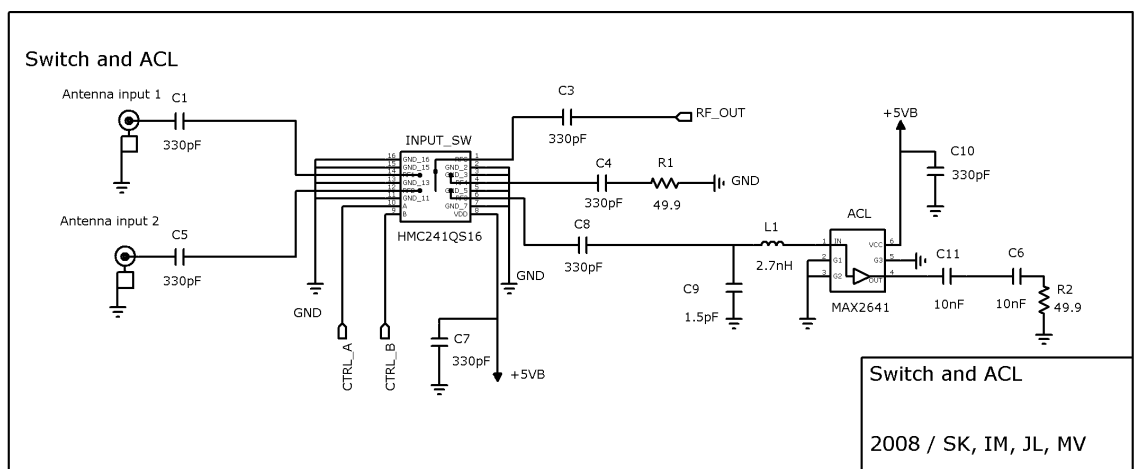

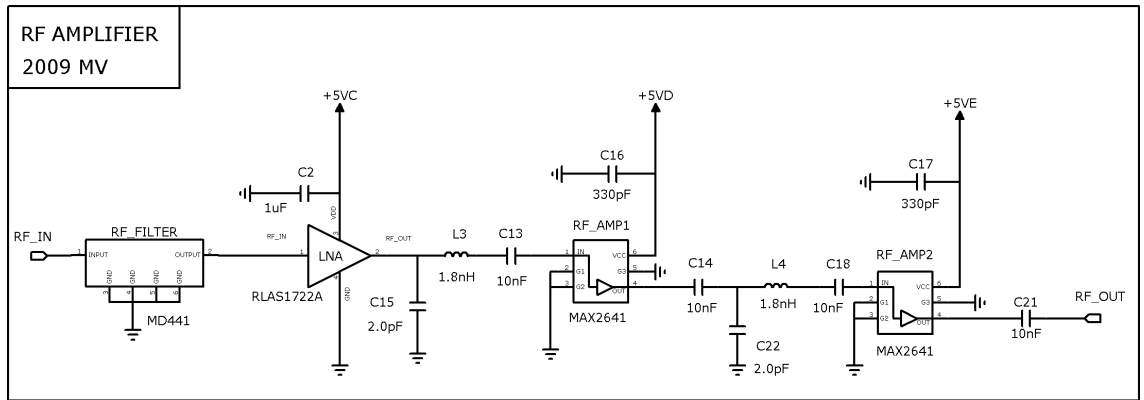*Figure 3.8 Input switch circuit schematic.*

Figure 3.9. RF amplifier circuit schematic.

solution is to leave the amplifier output port unmatched and match the input port as well as possible. The ACL output port is terminated with a 50 Ω chip resistor via DC blocking capacitors and the input is matched with an lumped components.

3.3.3 RF amplifier design

The RF amplifier functional block consists of the RF filter and three amplifier stages. The designed circuit is shown in Fig. 3.9. The RF filter and LNA ports are 50 Ω and therefore require no additional impedance matching elements. The two MAX2641 RF amplifiers have their inputs matched with lumped components. External DC blocking capacitors are placed around the MAX2641 amplifiers, while the LNA is internally DC blocked. Each amplifier is supplied with separate decoupled +5V DC.

3.3.4 Mixer design

Mixer design revolves around the MAX2681 downconverter mixer (Fig. 3.10). The RF
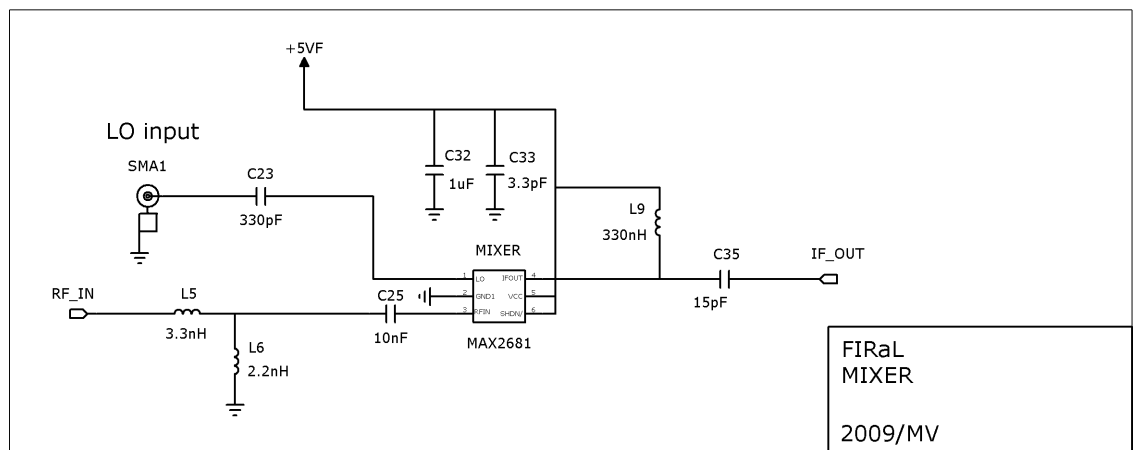

Figure 3.10. Mixer circuit schematic.

input is DC blocked with a capacitor and matched with lumped components. The LO input port return loss is less than -15 dB and doesn't therefore require a specific matching circuit. The IF output is matched with lumped components and the inductor L9 also provides bias voltage to the output pin. The output pin (pin 6) is not directly connected to the decoupled +5V power supply (pin 5), despite appearing to be so in Fig. 3.10.

3.3.5 IF amplifier design

The IF amplifier in Fig. 3.11 has pre- and post filters and two amplifier stages. The first filter requires input and output matching circuits, while the following amplifier needs DC blocking capacitors and bypassed +5V power supply. The second amplifier external components are necessary for biasing and DC blocking. The latter amplifier stage uses the mini-Circuit ERA-3+, instead of the MAX2650 amplifier, used in the preceding stage, because it has a higher output saturation power level. The output filter is a 3rd order butterworth band-pass filter, realised with lumped components [7].

3.3.6 Input switch control and power supply design

Fig. 3.12 shows the receiver PCB board interface to the RCB. The RCB measures the receiver board physical temperature with a PT100 sensor. A +5V power supply is distributed to the receiver active components via EMC filters [32]. The 2-bit input
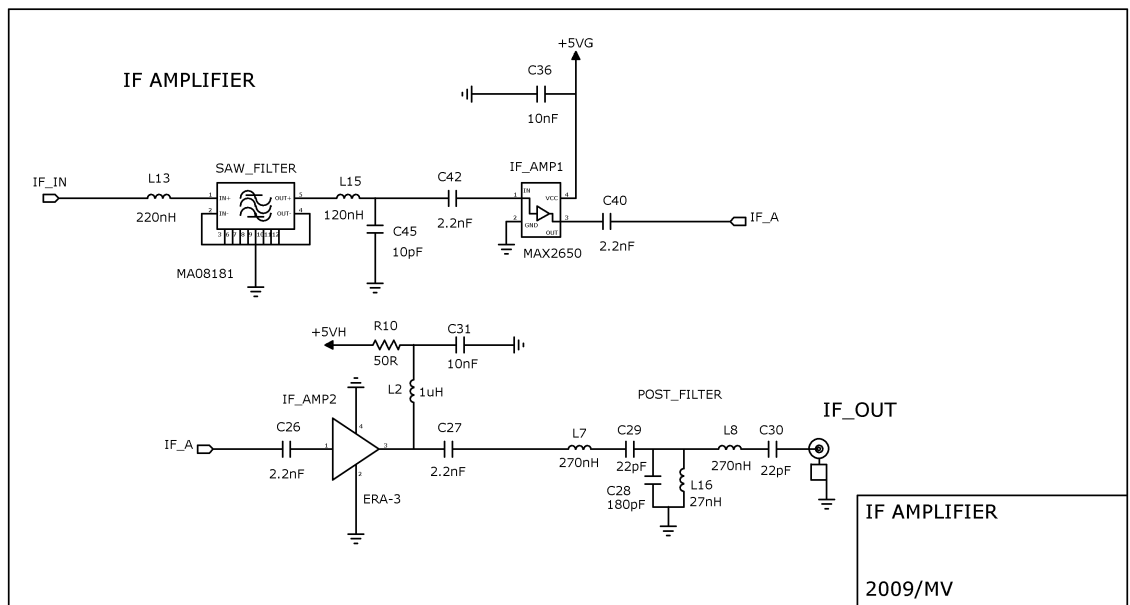

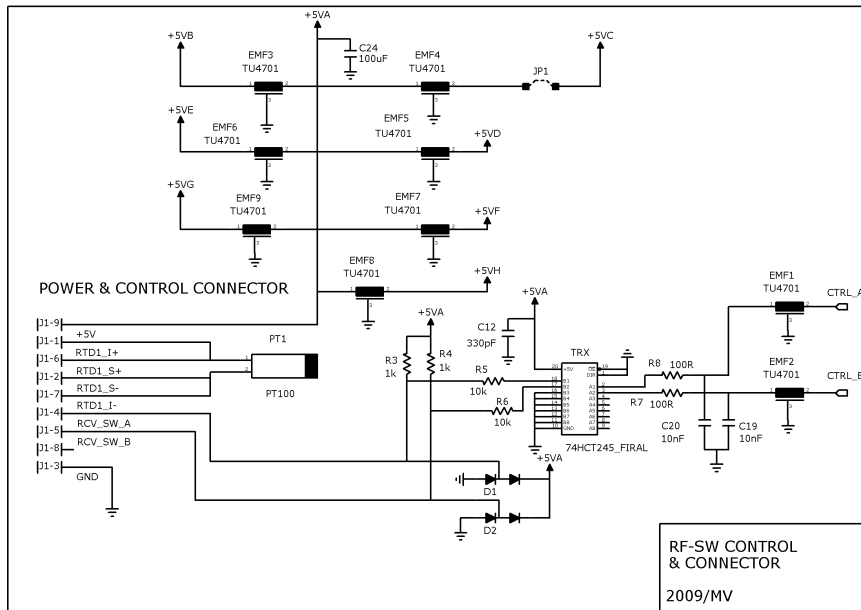*Figure 3.11. IF amplifier circuit schematic.*

Figure 3.12. Power supply and switch control circuit schematic.

switch control signal is transmitted from the RCB and received by a 74HCT245 non-inverting octal bus transceiver by Philips Semiconductor [33] and further transmitted to the input switch.

3.3.7 Receiver board layout design

The designed receiver PCB is shown in Fig. 3.13. Starting from the top right, the signal path continues counterclockwise to the bottom right. The input switch with calibration loads, RF filter and the LNA are housed in a separate enclosure in order to reduce interference from adjoining electronics. Similarly, the following two RF amplifiers, mixer and IF section are all separated from each other with metal walls. Power supply and switch control signals are distributed from the centre section to the enclosures through EMC filters. Signal integrity is further enhanced by filling the board periphery outside the traces and component pads with grounded copper. The bottom ground layer is connected to the top layer copper shield with plated vias. The vias are visible in Fig. 3.13 as dots.
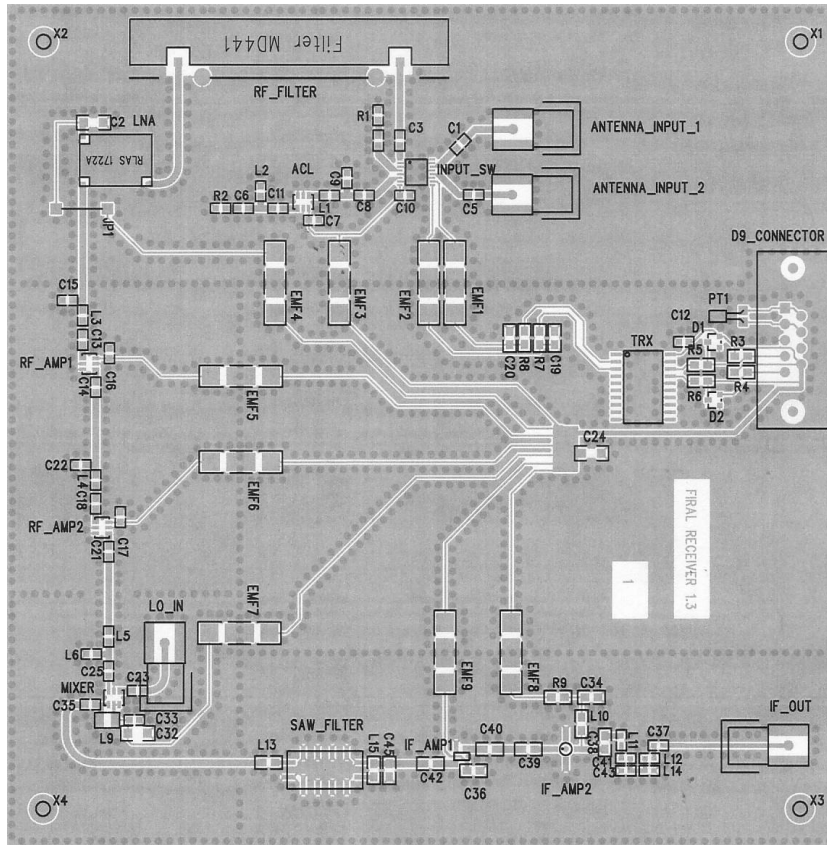
Figure 3.13. Receiver board top layer layout.

3.4 LO board design

The block level LO design is the same as in the HUT-2D instrument. A 147 mm x 147 mm x 1 mm Rogers 4350B PCB (ε_r = 3.48) is used for the LO realisation [34]. LO frequency parts of the LO board are realised with microstrip technology, similarly as with the receiver board design. A VCO (voltage controlled oscillator) by Mini-Ciruit [35], operating in the 1.960 – 2.350 GHz frequency range is used to produce the 1990 – 2050 MHz LO signal. Output power is around 0 dBm, as dictated by the receiver board MAX2681 mixer [26]. A programmable clock generator supplies a reference signal to a 256-to-1 prescaled single channel frequency synthesizer PLL chip, which then drives the VCO output to the desired frequency in 1 MHz steps. The LO board block diagram is shown in Figure 3.14. The reference clock generator outputs square wave signal, which has to be filtered before it can be used as the PLL reference signal. The
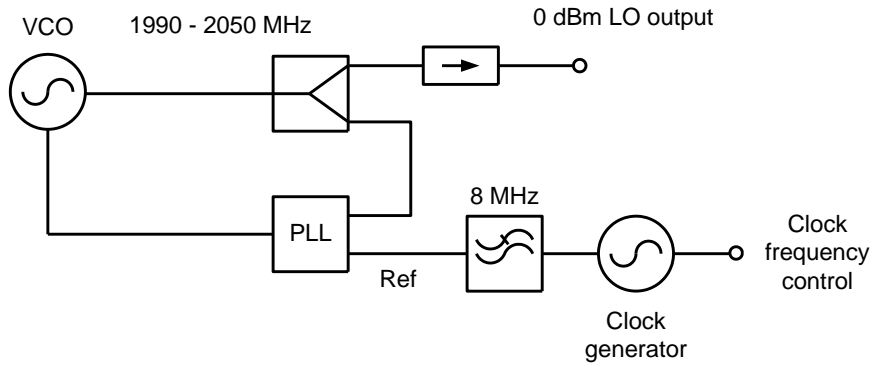
Figure 3.14. LO circuit block diagram.

VCO output signal is split in the 3 dB power divider to the PLL feedback loop and to the LO output. An isolator is placed in the LO output path in order to provide a degree of immunity from possible reflections arriving from mismatched load impedances.

3.4.1 Clock generator design

The VCO PLL reference signal is generated with an AMI Semiconductor FS6377-01 programmable 3-PLL reference clock generator [36]. The 256-to-1 prescaled single channel frequency synthesizer (PLL in Fig. 3.14) used in the main VCO PLL requires a 7.7734375 – 8.0078125 MHz reference signal in order to produce VCO output at 1990 – 2050 MHz. The clock generator output frequency is determined by an external crystal oscillator and 3 programmable frequency dividers. The output frequency f_{ref} value can be calculated as

$$f_{ref} = f_{crystal} \left(\frac{N_F}{N_R} \right) \left(\frac{1}{N_P} \right),$$ (3.10)

where $f_{crystal}$ is the crystal oscillator frequency and N_F, N_R, and N_P are the three divider moduli [36].

The clock generator design (Fig. 3.15) is realised with a 25 MHz crystal oscillator and other external components as recommended by [36]. The clock generator chip is programmed via a two signal-line I^{2}C bus [37]. The square-wave clock output signal is then buffered and the level shifted in a simple operational amplifier (op-amp) circuit. The reference clock signal is further processed in a 6th degree Sallen-Key type [38] 8 MHz low-pass Butterworth filter in order to attenuate the higher harmonics [39].
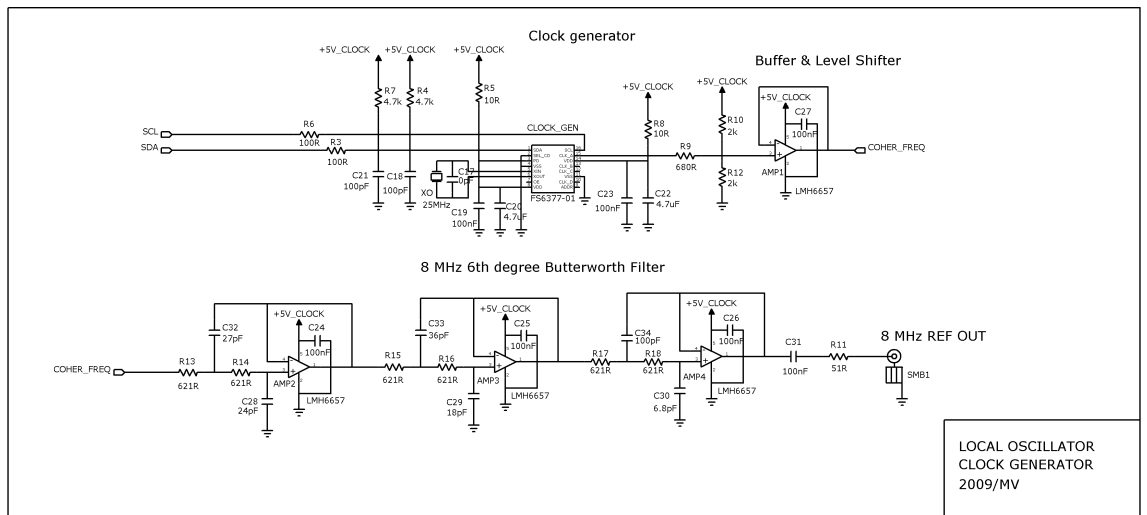
Figure 3.15. Clock generator circuit schematic.

Following the filter, the reference signal is DC blocked and the output impedance is set to 50 Ω.

3.4.2 VCO phase-locked loop design

The local oscillator is built around a Motorola MC12179 single channel frequency synthesizer [40]. The VCO frequency is divided by 256 and compared with the reference in a digital phase/frequency detector. The phase/frequency detector output is amplified by a charge pump and sent to the loop filter. The charge pump current output enables the use of a passive loop filter. The resulting tuning voltage drives the VCO to the desired output frequency. Required external functions for the synthesizer include the reference frequency signal, loop filter and VCO.

The PLL performance is determined by the reference and VCO frequency sideband noise performances and the choice of loop filter bandwidth. The loop filter bandwidth can be chosen based on three different considerations. If fast tuning speeds are required, the filter bandwidth should be maximised. In case the reference frequency sideband spurious signals are to be suppressed, the filter bandwidth should be minimised. It is also possible to choose the filter bandwidth in order to optimise the sideband noise performance. The latter approach is used in this work. [40]

The loop filter bandwidth is chosen by plotting the VCO and reference signal noise sideband spectra and selecting the point where the two curves cross in order to minimise the total sideband noise. Fig. 3.16 (a) shows a typical scenario. If the reference

oscillator signal is at a lower frequency than the VCO, it is necessary to add the resulting increase in phase noise due to frequency multiplication to the reference oscillator spectrum (or subtract from the VCO spectrum if it's frequency is divided). In the FIRaL LO board the VCO frequency is divided by 256, reducing the VCO phase noise by 20*log(256) = 48 dB. The PLL chip itself is a source of phase noise, increasing the reference signal phase noise by 15 dB [40]. Fig. 3.16 (b) shows the comparable phase noise spectrums of the VCO and reference oscillator. It is apparent from Fig. 3.16 (b) that the clock generator reference signal is mush noisier than a typical crystal reference and the two curves do not cross at all. For optimum noise performance, the FIRaL PLL loop filter bandwidth should be as close to zero as possible. Loop filter bandwidth of 2 kHz is chosen in order to keep the settling time reasonable (0.5 ms ideal).

The designed PLL circuit is illustrated in Fig. 3.17. For proper operation, a resistor (R1) is needed in place of the crystal oscillator, the reference port is DC blocked (C6) and the clock generator is isolated at the VCO frequency with a low-pass filter (L1 and C7).

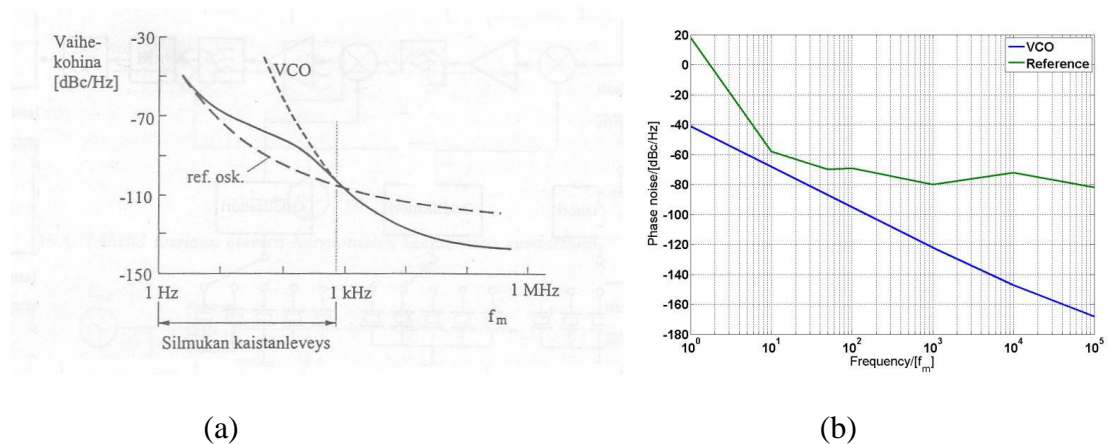(a)   (b)

Figure 3.16. Output phase noise spectra. (a) Typical curves for a VCO and crystal reference oscillator. The bandwidth is chosen to optimise the overall phase noise performance (solid line) [16]. (b) FIRaL LO reference oscillator and VCO phase noise spectra. VCO phase noise is taken from literature [35] and the clock generator reference is measured with a spectrum analyser.
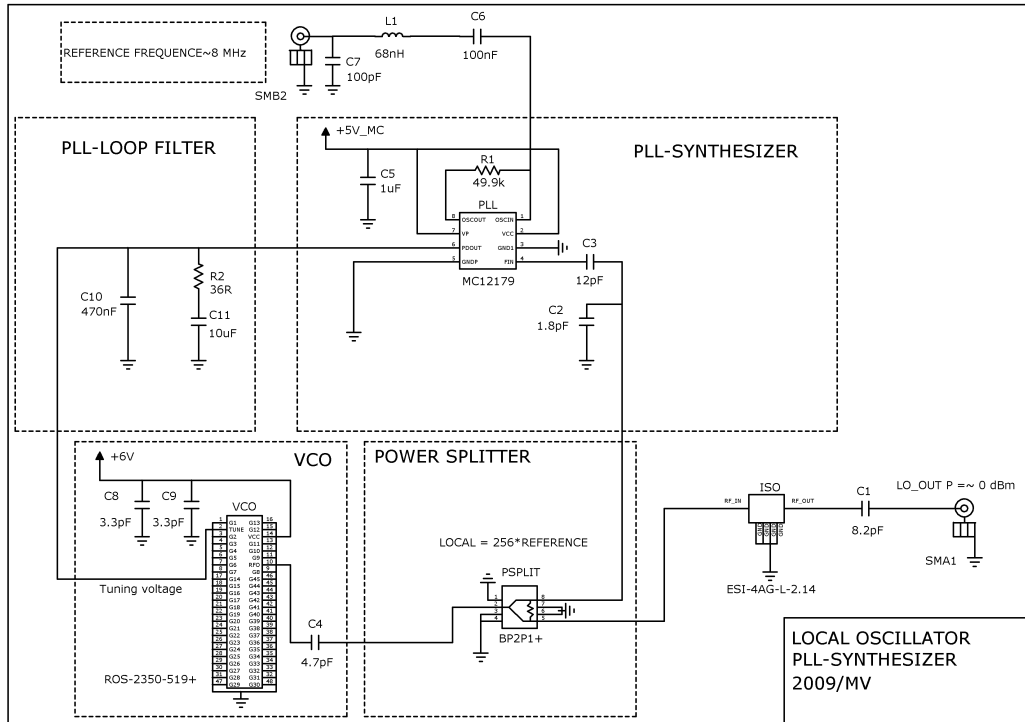
Figure 3.17. VCO PLL circuit schematic.

The 2 kHz 3rd order passive loop filter is implemented with a resistor and two capacitors [40], [41]. The VCO requires +6V DC for operation, +5V DC is fed to the other LO board integrated circuits (ICs). Otherwise, the VCO only has the tuning port and output port. VCO output signal is DC blocked before split into the PLL chip frequency prescaler input and to the output path. The PLL chip prescaler input is impedance matched with lumped components. LO board output is then fed through an isolator, DC blocked and finally taken out from an SMA connector.

3.4.3 LO board interface design

Fig. 3.18 shows the LO PCB interface to the RCB and control computer. The RCB provides the LO board with +5 V and +15 V DC power supply. The +15 V supply is regulated to +6 V DC to facilitate the VCO. The power supplies are decoupled from rest of the circuitry with EMC filters [32]. Two data lines for LO frequency control are connected to the clock generator via NFW31SP signal line noise suppression filters by Murata [42].
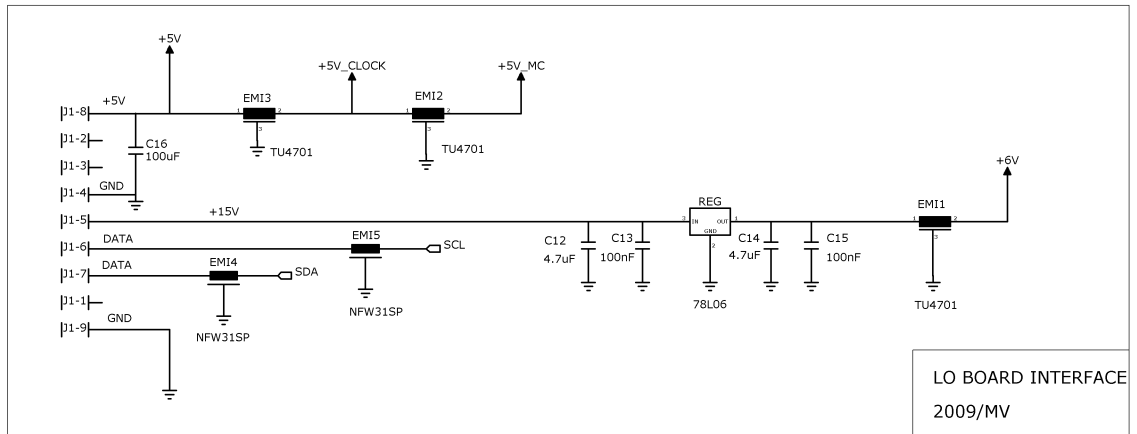
Figure 3.18. LO interface circuit schematic.

3.4.4 Receiver board layout design

The designed LO PCB is illustrated in Fig. 3.19. The PCB is divided into three EMC enclosures, with the left-hand side housing the main PLL. The right-hand side is further divided into the clock generator based reference signal electronics and the connector block which also houses the +6 V DC regulator. As with the receiver PCB, the board
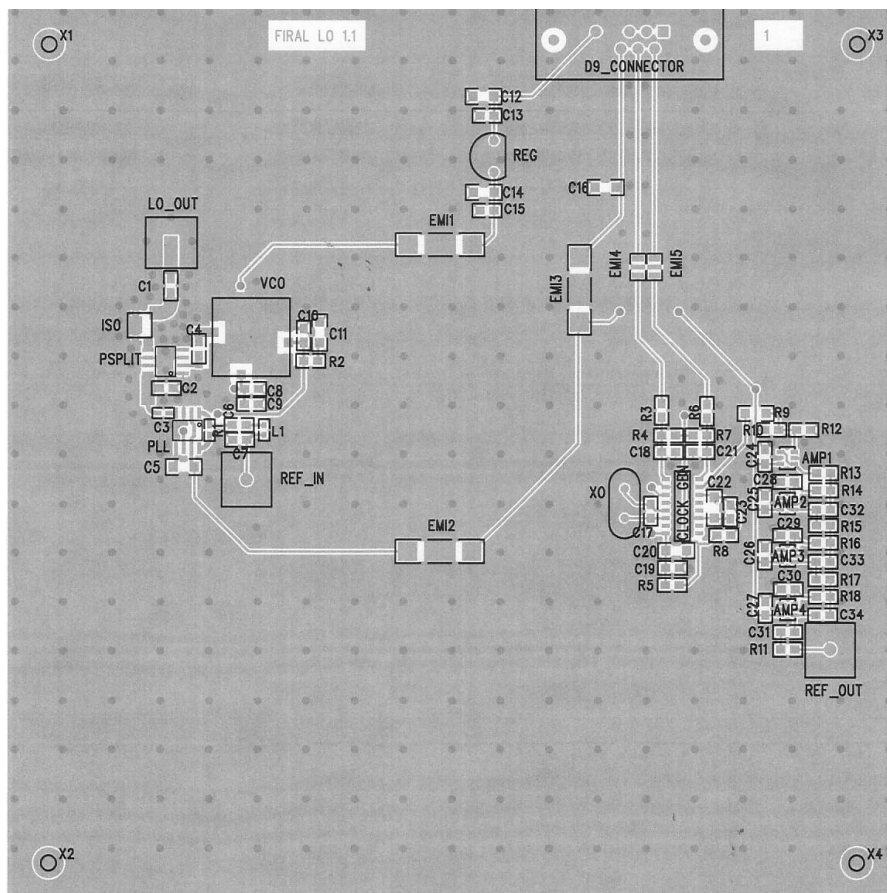

Figure 3.19. LO board top layer layout.

periphery outside the traces and component pads is shielded with grounded copper. The bottom layer is generally used as the ground plane, while being punctuated by a few low-frequency signal traces in order to facilitate the overall PCB layout design.

3.5 Antenna design

A horn antenna realisation is chosen in order to produce the specified 30 degree beamwidth in both E- and H-planes. A pyramidal horn is constructed from a WR-430 (a = 109.22 mm x b = 54.61 mm) rectangular waveguide section and an extension with linearly increasing cross section in the axial direction. The UMTS radio system operates at vertical polarisation and the horn antenna is designed to couple the E-plane direction radio emissions to the antenna feed cable. Center frequency free-space wavelength is λ = 153.85 mm. The dominant TE_{10} propagation mode wavelength λ_g in the WR-430 waveguide is

$$\lambda_g = \frac{\lambda}{\sqrt{1 - \left(\dfrac{f_c}{f}\right)^2}} = 216.50 \, \text{mm}, \tag{3.11}$$

where f_c is the TE_{10} mode cutoff frequency (1.372 GHz) [17], [43]. The waveguide

(a)   (b)

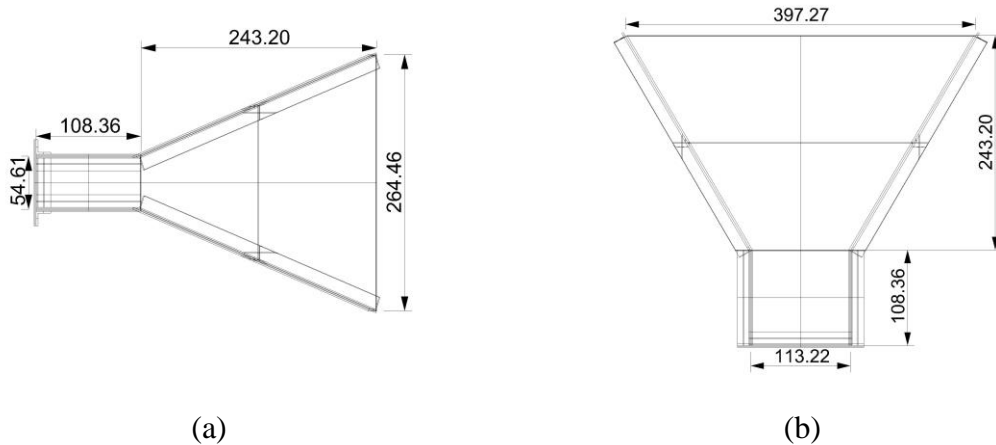*Figure 3.20. Designed horn antenna internal dimensions. Waveguide E-plane height a = 54.61 mm, waveguide H-plane width b = 109.22 mm, waveguide length l = 108.36 mm, horn depth R = 243.20 mm, horn aperture E-plane height B = 264.46 mm, and horn aperture H-plane width A = 397.27 mm. (a) Pyramidal horn antenna side-view. (b) Pyramidal horn antenna top-view.*
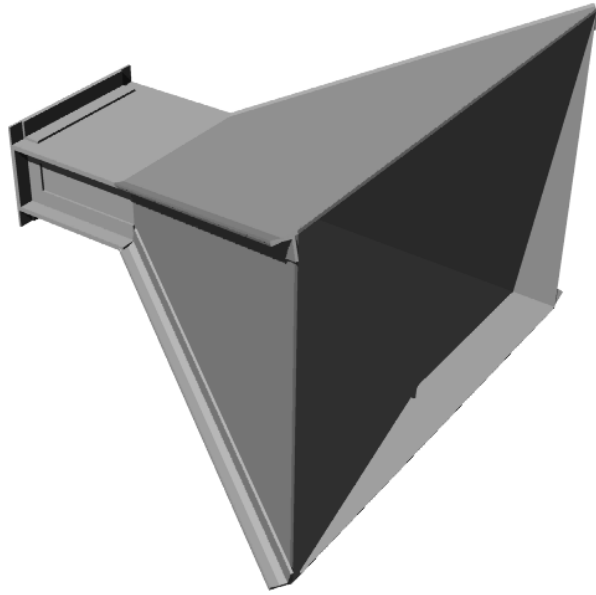
Figure 3.21. An artistic view of the designed antenna.

section is $\lambda_g/2$ long and has a $\lambda/4$ length E-plane direction probe placed in the middle of the waveguide bottom sheet in order to match the 50 Ω antenna feed cable to the antenna. One end of the waveguide is short-circuited and the other end is attached to the pyramidal horn extension.

The pyramidal horn horn is designed according to a published method which enables to find the physical horn dimensions based on the required half-power beamwidth [44]. The method involves solving the two principal plane quadratic phase distribution constants [45] t (H-plane) and s (E-plane) iteratively. The horn aperture dimensions A and B along with the horn depth R can then be calculated with the knowledge of the desired half-power beamwidth. The designed antenna with dimensions is shown in Fig 3.20. The antenna is construction is further illustrated in Fig. 3.21. A 2 mm thick aluminium plate is used for wall material and the structure is held together by riveting the plates to L-shaped aluminium profiles.

4 Laboratory measurements of the radiometer system

The radiometer system is constructed according to the design presented in Chapter 3. Prior to actual on-site measurements, the radiometer components and operation are tested in laboratory conditions. The most important parameters of the radiometer are the receiver input noise temperature, gain and IF bandwidth, on which the radiometer output voltage is directly dependent. Measurement sensitivity and stability are studied by measuring the output for several hours. Radiometer subsystems are also tested, including the LO output power, LO spectral quality, antenna radiation patterns, antenna gain, and receiver board antenna input return loss. Additionally, overall functionality of the radiometer control software and hardware operation is tested.

4.1 Receiver board measurements

The most important parts of the receiver board electronics are the input switch and RF amplifier functional blocks, since they mainly determine the receiver input noise temperature and house the internal calibration loads. The performance evaluation of the receiver input sections is conducted by measuring the input return loss. Measurements are performed with an Agilent Technologies 8753ES network analyser, which has a specified reflection coefficient measurement uncertainty of $\pm$ 0.02 dB or better in the FIRaL operating frequency [46]. Fig. 4.1 shows the measured input port reflection
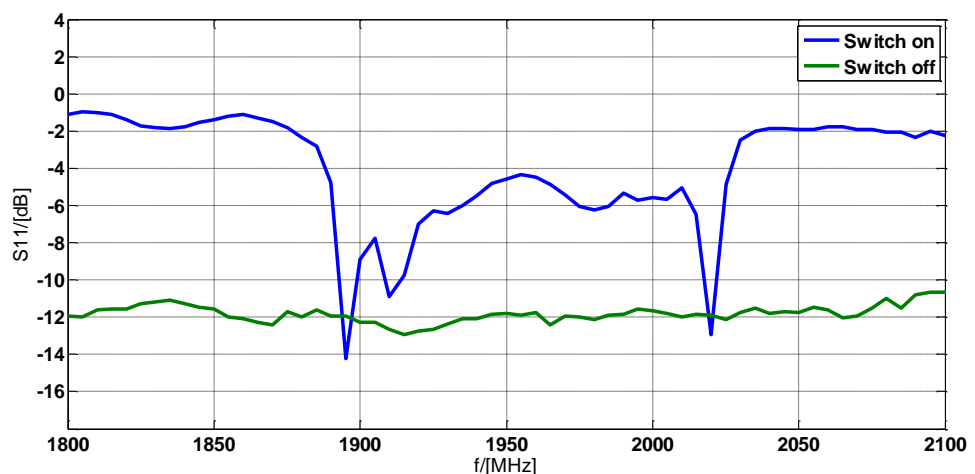

Figure 4.1. Antenna input port return loss with the input switch closed (on) or open (off).

coefficient with the front-end switch either switched on or off. The return loss is around 12 dB with the switch in the "off" state. The documented "off" state" input return loss for the used switch is 12 dB or better in the receiver operating frequency [22], which implies that the designed input switch circuit is operating properly.

For the switch "on" state, the reflection coefficient of the antenna port in Fig. 4.1 is -4.3 dB or 0.59 at the highest point in the radiometer operating band of 1920 – 1980 MHz. In this state, the switch is nearly transparent and the receiver input port is in essence directly connected to the RF filter input. Therefore, the measured input return loss of 4 dB is much higher than anticipated, since the documented input return loss of the RF filter and LNA are 18 dB and 22 dB, respectively [23], [24]. It is suspected that the RF filter and LNA port impedances are not as well matched as specified and are cause of the high input reflection coefficient. NSN, the provider of RF filter and LNA components, confirmed that they have had similar results in applying these components. The component placement and circuit layout is critical and it has required further circuit layout development from the LIME project corporate partner NSN for them to reach the level of performance as spesified by datasheets. Unfortunately, this information was not available during the design of the FIRaL radiometer and the only option within the LIME project is to complete the radiometer despite the unideal performance of the RF amplifier section.

The RF filter and LNA port impedance mismatches have a number of implications. Firstly, the gain of the receiver is diminished as a part of the input noise power is reflected back and the effective loss also increases the radiometer input noise temperature. Secondly, the use of the internal calibration loads becomes unfeasible as the effective noise temperature of the calibration loads is affected by the multiple reflections arising from the impedance mismatches and causes uncertainty in the calibration of the calibration loads. Thirdly, stability of the receiver might become compromised during long measurements as small changes in the RF port impedances can alter the receiver gain and input noise temperature.
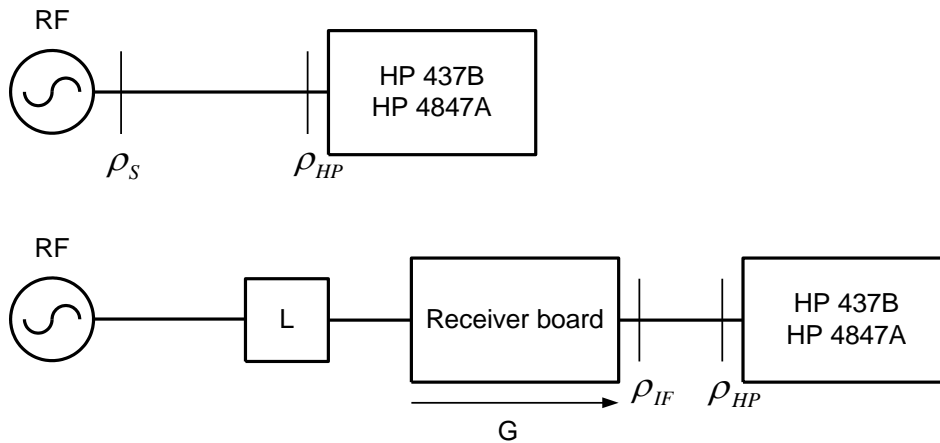
Figure 4.2. Receiver gain measurement setup.

4.1.1 Receiver gain

The receiver gain is measured by injecting a known level of microwave power to the antenna input and monitoring the IF output power level with a power meter. The measurement setup is depicted in Fig. 4.2. A Rohde & Schwarz SMR 60 signal generator is used as the source, and the test signal and IF power are measured with a HP 437B power meter and HP 8487A power sensor. The source power level is first measured by connecting the generator and power meter directly. Next the test signal is fed to the receiver via an attenuator and the IF power level is measured. A total amount of 70 dB attenuation is inserted between the signal generator and receiver in order to avoid overloading the receiver electronics. The insertion loss of the measurement cables and coaxial attenuators are measured with the 8753ES network analyser and results are corrected accordingly. The corrected measurement results are shown in Fig. 4.3.
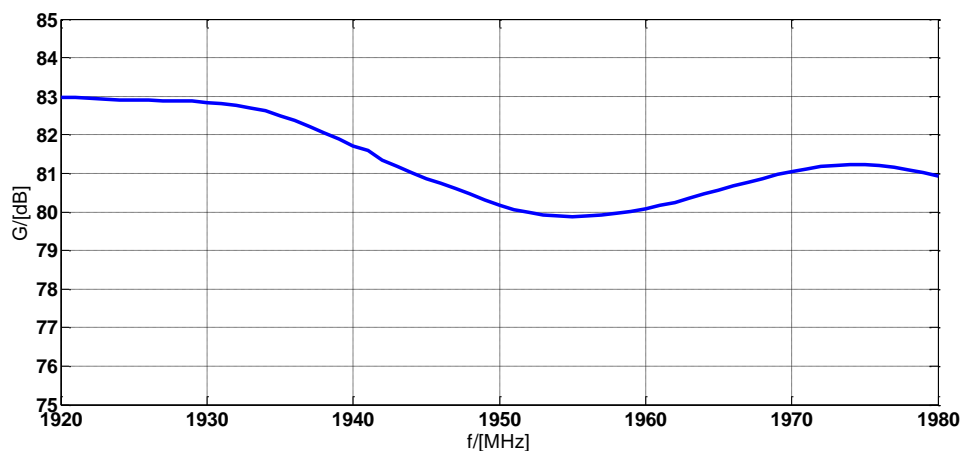

Figure 4.3. Measured receiver gain.

Measurement uncertainty of the test signal power is caused by the power meter calibration error (1 %), random errors (0.34 %), and the error caused by the reflection coefficients of the generator and meter, ρ_S (0.33) and ρ_{HP} (0.02), respectively. In the measurement of IF output power, the multiple reflections caused by the impedance mismatches of the signal generator and receiver input board are effectively suppressed by the attenuator. Remaining significant measurement error sources are those of random nature, error in the measurement of attenuator insertion loss (2.3 %), and errors due to the reflection coefficients of the meter and IF output port (ρ_{IF} = 0.50). The detailed analysis of measurement uncertainties due to multiple sources is not presented here. The theory and analysis of measurement uncertainties is presented in [47] and application examples can be found in [48]. The calculated measurement uncertainty is ± 0.2 dB with confidence interval of 95%. The maximum receiver gain is 83.0 ± 0.2 dB at 1920 MHz and the minimum is 79.9 ± 0.2 dB at 1955 MHz. The total gain variation in the receiver operating band is 3.1 ± 0.3. The realised receiver board gain falls within specifications and will provide an IF signal at an appropriate level for the square-law detector.

4.1.2 IF amplifier bandwidth

The IF amplifier S-parameters are measured with the 8753ES network analyser, from which the IF filter 3 dB bandwidth can be found. The test signal was coupled to the IF amplifier input via an SMA connector which was temporarily soldered to the receiver board and the IF amplifier standard output connector is used as the measurement output port. The measurement results are shown in Fig. 4.4. Measurement uncertainties in the
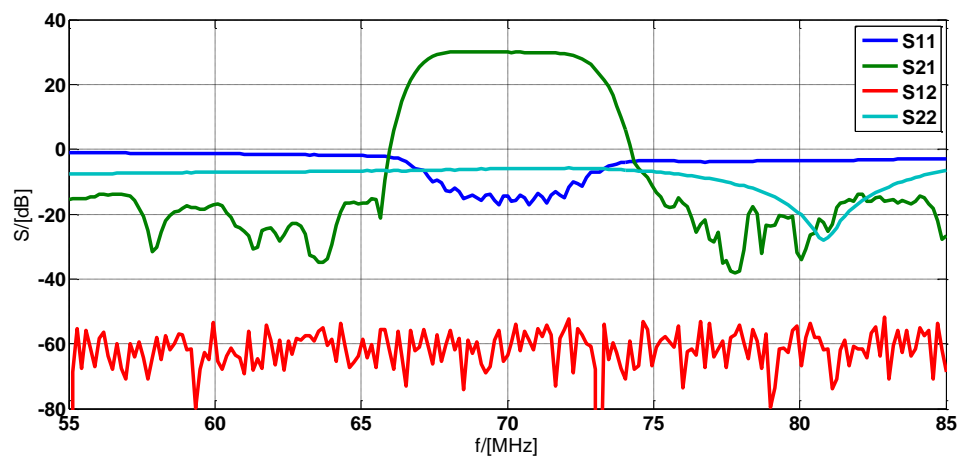

Figure 4.4. Measured IF amplifier S-parameters.

reflection and transmission responses are ± 0.02 dB and ± 0.1 dB, respectively [46]. Maximum gain of 30.15 ± 0.1 dB occurs at 68.65 MHz. The resulting 3 dB bandwidth is 5.468 ± 0.035 MHz. Spesified 3 dB bandwidth is 5.5 MHz and the measurement result is in agreement [27]. The IF amplifier center frequency is found to be 69.894 ± 0.012 MHz, by taking the geometric mean of the S21 -3 dB bandwidth boundary frequencies. Measured IF amplifier input and output reflection coefficients are -7.12 ± 0.02 and -5.80 ± 0.02 dB, respectively, at the highest in the IF amplifier bandwidth. Reverse transmission S12 is below the network analyser noise floor.

4.2 LO board measurements

Significant parameters of the LO subsytem are the LO output power and phase noise of the output spectrum. The LO output power is measured with the HP 437B power meter and HP 8487A power sensor via an extension cable. The power meter calibration introduces measurement uncertainty (1 %). Other sources causing measurement uncertainty are the extension cable insertion loss measurement (± 0.1 dB) and the reflection coefficients ρ_{LO} (0.5) and ρ_{HP} (0.02) of the LO board output port and power meter sensor input, respectively. Random variation in the power meter reading was suppressed by averaging the measurement 32 times. Total measurement uncertainty is ± 0.2 dB at 95 % confidence interval. The measured LO output power is shown in Fig. 4.5. The LO power level is 2.0 ± 0.2 dBm at the lowest and 2.7 ± 0.2 dBm at the highest. The realised LO output power is at a suitable level for the receiver board mixer stage. The LO output signal phase noise spectrum measurement results are collected in Table 4.1. According to the phase noise measurement results, the LO output spectrum is
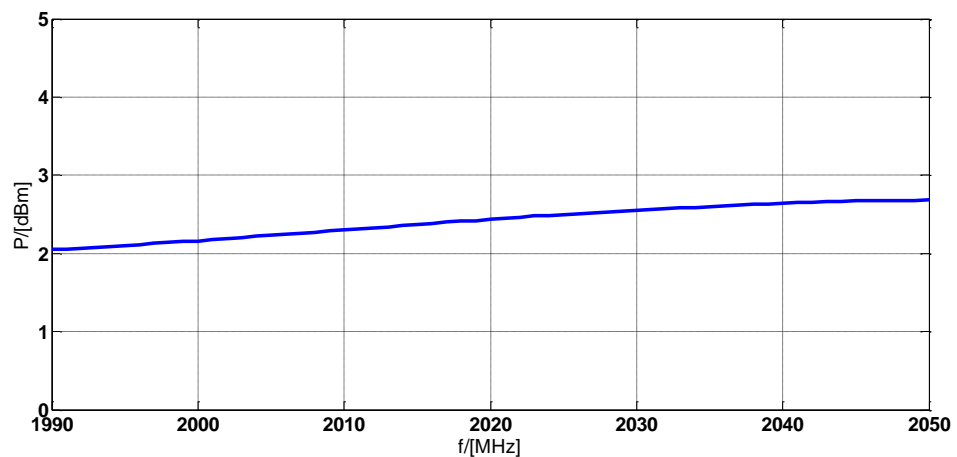

Figure 4.5. Measured LO output power.

Table 4.1 LO output phase noise spectrum

Frequency (kHz)	1	10	100	1000
Phase noise (dBc/Hz)	-48	-71	-98	-137

somewhat noisy and would not perhaps perform well in a typical communications receiver. The results are expected as the clock generator PLL reference signal is quite noisy. However, for measuring noise-like RF signals, the realised LO output signal spectrum is adequate.

4.3 Antenna measurements

Antenna measurements are performed in order to quantify the antenna half-power beamwidths in azimuth (θ_{az}) and elevation (θ_{el}) direction, input impedance matching, antenna gain G_a, and radiation efficiency η_l.

4.3.1 Antenna input impedance matching

The antenna input impedance matching is measured with the 8753ES network analyser, by placing the antenna in an anechoic chamber and measuring the antenna input reflection coefficient ρ_a. The most significant measurement error source causing measurement uncertainty is the network analyser residual error of $\pm$ 0.02 dB [46]. The measurement result is shown in Fig. 4.6, while noting that S11 is equal to the magnitude of ρ_a. The antenna input reflection coefficient is -16.77 $\pm$ 0.02 dB or better in the radiometer operation band.
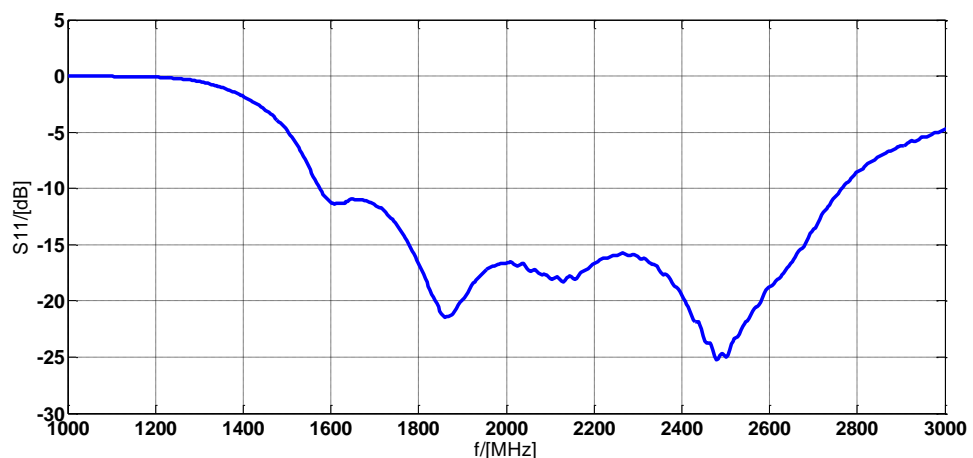

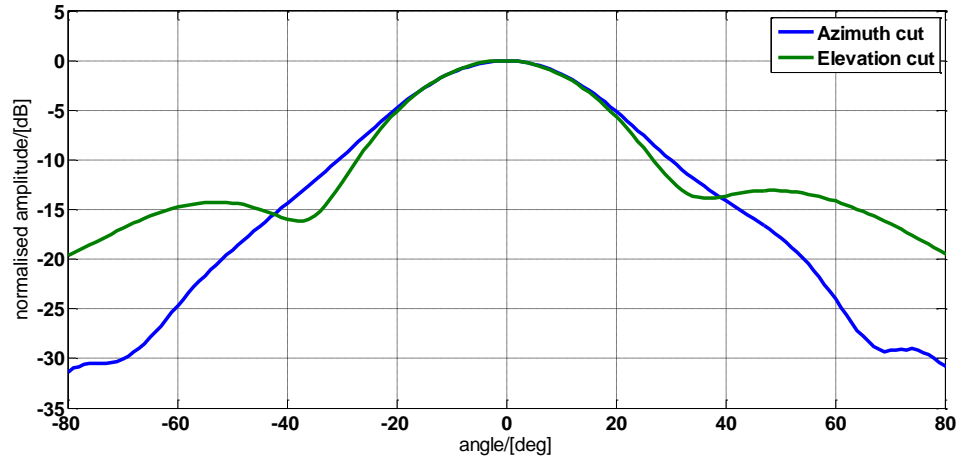*Figure 4.6. Measured antenna input reflection coefficient.*

Figure 4.7. Measured azimuth and elevation direction antenna pattern cuts.

4.3.2 Antenna radiation pattern

The antenna half-power beamwidth is studied by measuring the antenna radiation patterns in azimuth and elevation directions in an anechoic chamber (i.e. free-space antenna range) with the far-field method [49]. Fig. 4.7 shows the measured radiation patterns. Designed half-power beamwith is 30° in both E- and H-planes and the realised values are 30.8° ± 0.2° and 30.3° ± 0.2°, respectively. Random measurement uncertainty is ± 0.07° and ± 0.06° in the two directions. Taking in consideration possible mesurement uncertainty due to amplitude tapering in the illuminating plane-wave, antenna impedance matching, polarisation matching, and antenna alignment, the total measurement uncertainty is estimated to be ± 0.2° in both directions with confidence interval of 95 %. The realised antenna is considered to be usable in the light of the design specifications.

Knowledge of the main E- and H-plane half-power beamwidth allows the estimation of antenna directivity. Directivity is defined to be 4π times the ratio of the power radiated per unit solid angle in the direction of maximum radiation to the total power radiated by the antenna [49]. The exact calculation of directivity requires knowledge of the antenna radiation pattern over the 4π solid angle. For a rectangular aperture antenna, such as a horn with an uniform amplitude distribution in the E-plane and a cosine amplitude taper in the H-plane, the directivity can be estimated to be

$$D = \frac{35230}{\theta_{az}\theta_{el}}, \tag{4.1}$$

where the beamwidths are in degrees [50]. Estimated directivity is, therefore, 37.75 or 15.8 dB. Calculated measurement uncertainty is ± 0.04 dB [47]. In conclusion, it is estimated that the directivity is 15.8 ± 0.1 dB with confidence interval of 95 %.

4.3.3 Antenna gain

The pyramidal horn antenna gain is determined with a gain-transfer measurement, in which the gain of the antenna under test (AUT) is compared to the gain of a standard gain antenna. The gain of the AUT G_a is

$$G_a = \frac{P_a}{P_{ref}} G_{ref}, \tag{4.2}$$

Where P_a is the received power level with the AUT, P_{ref} is the received power level with the standard gain antenna and G_{ref} is the gain of the standard gain antenna [16]. Estimated measurement uncertainties of the power levels are similar as in the directivity measurement (± 0.1 dB) and the standard gain horn gain is 9.4 ± 0.25 dB [51]. The measured power ratio P_a/P_{ref} is 5.76 dB and the calculated AUT gain is, therefore, 15.2 ± 0.3 dB, with confidence interval of 95 %.

Part of the input power accepted by the antenna is lost as dielectric and conductive losses. The losses can be quantified with the antenna radiation efficiency η_l, which is defined as the ratio of gain and directivity as

$$\eta_l = \frac{G}{D}. \tag{4.3}$$

The calculated radiation efficiency of the designed pyramidal horn antenna is 0.87 ± 0.07, with confidence interval of 95 %.

4.4 Radiometer calibration

In order to determine the detector offset, radiometer gain, and receiver input noise temperature, the detected output power is measured in four different scenarios. The measurement setup is shown in Fig. 4.8. The detected power is first measured with a hot
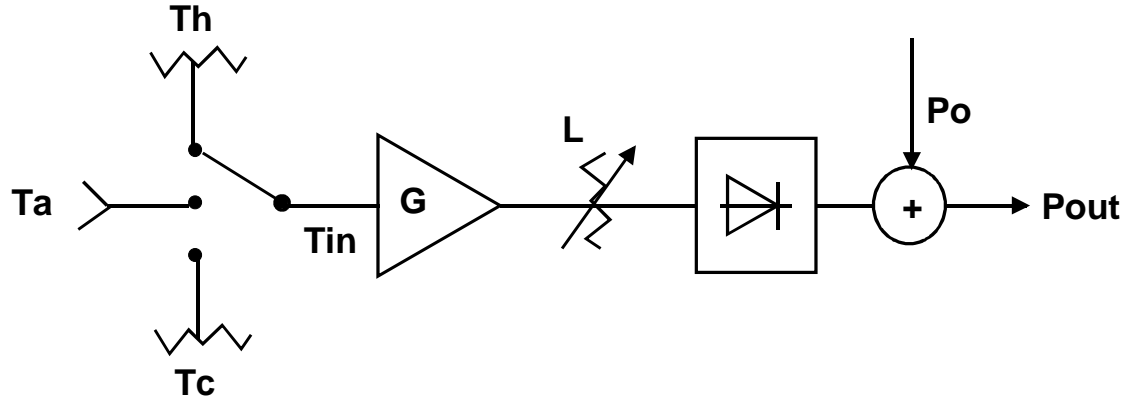
Figure 4.8. Measurement setup in radiometer calibration [52].

calibration load placed at the receiver input and then with a cold calibration load. A second set of similar measurements are performed with the hot and cold calibration loads, while also placing an attenuator at the end of the IF chain and again monitoring the detected output power. The output of the RCB square-law detector is of the form

$$\overline{V}_{out} = V_0 + g\left(T + T_{REC}\right),\tag{4.4}$$

where V_0 is the detector offset, T is the equivalent noise temperature of a matched load, and g is the total gain of the radiometer. From Eq. (2.22), $g = g_{LF}C_dG$. A set of four equations from Eq. (4.4), with four unknown parameters of receiver input noise temperature, radiometer gain, detector offset, and attenuator loss, are formulated and solved. The IF attenuator must be placed before the square-law detector diodes so that the detector offset does not change. Furthermore, the IF attenuator must be placed at the end of the receiver chain so that the effect on the receiver input noise temperature is negligible. The RCB has a programmable attenuator before the detector in order to facilitate calibration. [52]

4.4.1 Receiver input noise temperature

The receiver input noise temperature is measured with the aforemention method. The hot calibration load is a 50 Ω SMA microwave termination at room temperature T_h = 292.0 K. The termination temperature is measured with a calibrated precision digital thermometer Therm 2230-1 by Ahlborn Messtechnik, Germany, which has an estimated absolute accuracy of ± 0.1 ℃. The cold calibration load is a 50 Ω SMA microwave termination, which is submerged in boiling liquid nitrogen at T_{LN} = 77.4 K. The cold

termination is connected to an insulated 255 mm long coaxial cable and the other end of the cable is at room temperature. The effect of the cable on the cold load temperature is taken into account by measuring the cable loss beforehand and monitoring the cable temperature at 6 points with PT100 sensors during receiver calibration. The PT100 temperature sensors are placed equidistantly and with the knowledge of the cable loss per segment $L_c = 1.007$, the cold calibration load temperature T_c can be calculated as

$$T_c = \frac{T_{LN}}{L_c^6} + \frac{T_6}{L_c^6}\left(L_c - 1\right) + \frac{T_5}{L_c^5}\left(L_c - 1\right) + \frac{T_4}{L_c^4}\left(L_c - 1\right) + \frac{T_3}{L_c^3}\left(L_c - 1\right)$$
$$+ \frac{T_2}{L_c^2}\left(L_c - 1\right) + \frac{T_1}{L_c}\left(L_c - 1\right),$$

(4.5)

where T_n is the measured temperature of a cable segment and index $n = 1$ is at room temperature and $n = 6$ closest to the liquid nitrogen. The calculated cold calibration load temperature is $T_c = 83.3 \pm 1.6$ K at 1950 MHz, with confidence interval of 95 %.

Based on the calculated calibration load temperatures, the resulting receiver input noise temperature T_{REC} is as shown in Fig. 4.9. The measured receiver noise temperature is at a minimum of 457 K at 1957 MHz and at a maximum of 661 K at 1934 MHz. The receiver noise temperature is estimated to be within the dashed lines in Fig. 4.9, based on the calculated root-sum-square (RSS) total uncertainty [47]. The measurement uncertainty of the receiver noise temperature is discussed in the next section. The measurement uncertainty depends on the receiver and detector linearities, detector integration time, stability of the receiver stability, and the accuracy in which the calibration load temperatures are known. In the case of the FIRaL radiometer, the
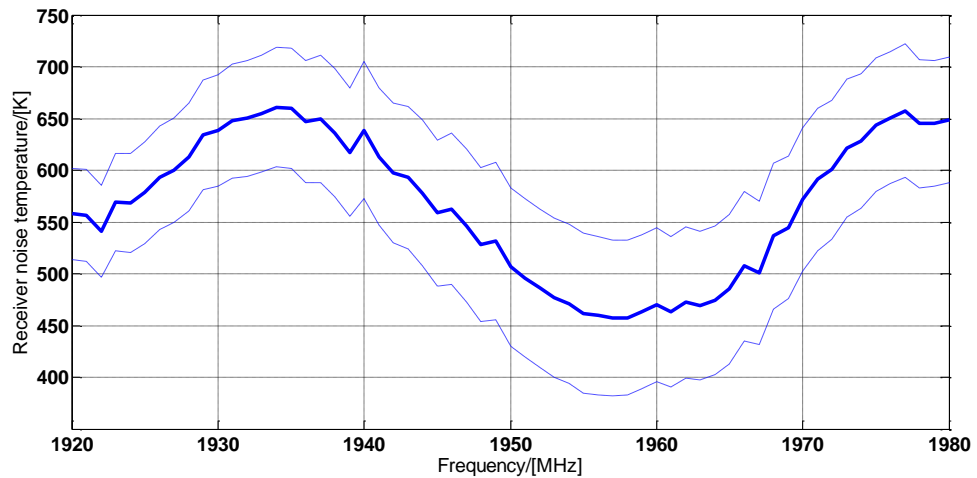

Figure 4.9. Receiver noise temperature.

calibration load temperature uncertainty is the most significant factor, because the receiver input impedance mismatch causes additional uncertainty to the calibration load temperatures.

4.4.2 Receiver input noise temperature measurement uncertainty

In Fig. 4.9, the effect of the measurement cable between the receiver input and calibration load and also the effect of the calibration load and receiver input reflection coefficients have been taken into account. In the receiver input noise temperature measurement, the actual measurement setup is similar to the network in Fig. 4.10. Using the notation in Fig. 4.10, T_G is the temperature of the noise generator (hot or cold calibration load), T_R is the equivalent noise temperature generated by the receiver towards the generator, which would be absorbed in to a matched load at the receiver input, and T_{IN} is the noise temperature of the net power delivered to the receiver. Z_{01} and Z_{02} are the port 1 and 2 impedances (50 Ω) and R_G and R_R are the generator and receiver input reflection coefficients, respectively. The connecting 2-port network is a coaxial waveguide with SMA connectors. R_{1S} and R_{2S} are the port 1 and 2 reflection coefficients while looking towards the connecting 2-port, respectively. [6]

The noise temperature of the net power delivered to the receiver is

$$T_{IN} = \Gamma \mathrm{T} T_G + \Gamma(1-\mathrm{T})T_{phys} + (1-\Gamma)T_R, \tag{4.6}$$

where Γ is mismatch loss factor and T is transmission factor. The first term in the right side of Eq. (4.6) is the net delivered noise temperature from the generator, the second
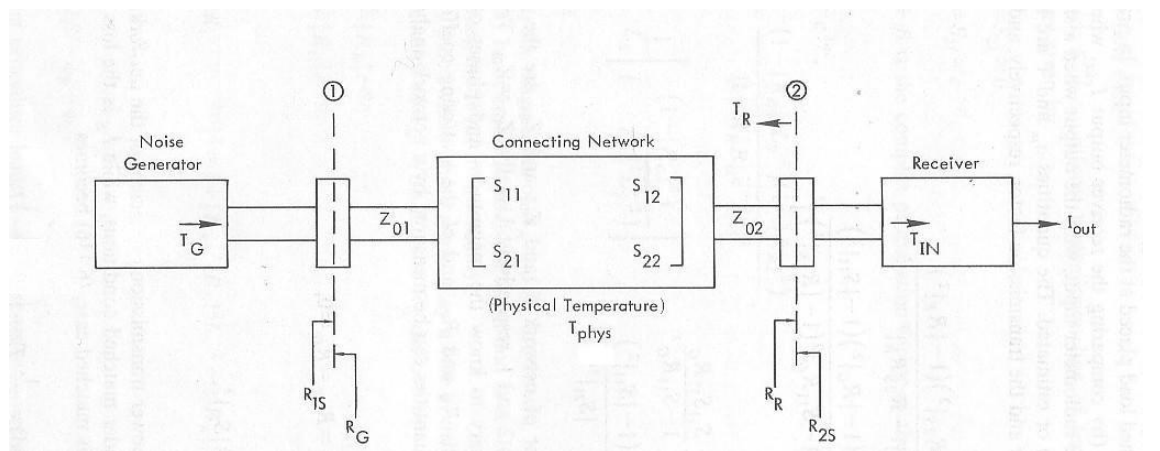

Figure 4.10. Receiver front end network [6].

58

term is the net delivered noise temperature arising from the self-emission of the connecting cable, and the third term is the net delivered noise temperature generated by the receiver towards the noise generator which is then reflected back towards the receiver. In the case where the 2-port network is a uniform transmission line and $S11 = S22 \approx 0$, the mismatch loss and transmission factors Γ and T, respectively, are of the form

$$\Gamma = \frac{\left(1-|R_G|^2 L_S^{-2}\right)\left(1-|R_R|^2\right)}{1+|R_R|^2|R_G|^2 L_S^{-2} - 2|R_R||R_G|L_S^{-1}\cos\theta}, \tag{4.7}$$

$$T = \frac{1}{L_S}\left[\frac{\left(1-|R_G|^2\right)}{\left(1-|R_G|^2 L_S^{-2}\right)}\right], \tag{4.8}$$

where

$$L_S = \frac{1}{|S_{21}|^2}, \tag{4.9}$$

and angle θ can take any value from 0 to π. [6]

In the FIRaL receiver calibration, at 1950 MHz, $/R_G/ = 0.027 \pm 0.008$ or 0.005 ± 0.001, where the first value is for the cold load and the second is for hot load, $/R_R/ = 0.59 \pm 0.02$, and $L_S = 1.199 \pm 0.014$. Let us consider the case when the cold calibration load of $T_G = 83.3 \pm 1.6$ K is measured. If, based on the receiver board physical temperature, T_R is estimated to be 315 ± 20 K, the noise temperature of the net power delivered to the receiver is 157.8 ± 11.8 K according to Eqs. (4.6) − (4.9). The contribution of the last term in the right side of Eq. (4.6) is 110.7 K (mean value), which means that most of the net delivered noise power is caused by the backward noise radiation of the receiver, which is then reflected back toward the receiver. From Eq. (4.6), the noise temperature of this noise radiation is proportional to $(1 - \Gamma)T_R$. A large value of the mismatch loss factor Γ means that for reliable determination of term $(1 - \Gamma)T_R$, the amount of receiver backward noise radiation temperature T_R must be accurately known. Without reliable prior knowledge of the receiver noise temperature T_{REC}, the actual value of T_R is difficult to measure, which causes additional measurement uncertainty of the receiver noise temperature calibration. Another consequence of the lack of receiver noise

temperature calibration accuracy is that the equivalent noise temperatures of the internal calibration loads cannot be reliably determined. It is therefore decided that for on-site measurements external calibration loads are used.

Nevertheless, an estimate of the measurement uncertainty of the receiver input noise temperature can be formulated. As with the cold load, a similar analysis of the noise temperature of the net delivered noise power to the receiver by the hot calibration load is performed. With the known effective hot and cold calibration load temperatures, a set of measurements are conducted according to the IF attenuator calibration method [52]. The results are shown in Fig. 4.9 and the resulting RSS measurement uncertainty is at worst $\pm$ 78 K in the radiometer operating band.

The measured receiver input noise temperature of 457 K to 661 K is larger than the value of 175.2 K calculated in Chapter 3. The difference between the result and the prediction and also the variation within the the operating band is a direct consequency of higher than anticipated frequency dependent losses in the RF front end. The variation in the input noise temperature in Fig. 4.9 is most likely caused by corresponding variation in the RF filter effective insertion loss. If the noise temperature of the receiver cascade is calculated with Eq. (2.17) and the gain values of the input switch and RF filter in Table 3.1 are replaced by -1.0 dB and -2.6 dB, respectively, the resulting theoretical input noise temperature is 464 K. Similarly, if the input switch gain is -1.0 dB and the RF filter gain is -3.6 dB, the resulting noise temperature is 660 K. It is reasonable to assume that a similar mechanism as was demonstrated above causes the higher than anticipated receiver input noise temperature measurement results.

4.5 Radiometer stability and sensitivity

The radiometer sensitivity and stability is studied after calibration by measuring a matched load at room temperature for several hours at 1930 MHz. The results are shown in Fig. 4.11. As seen from the figure, the radiometer output is quite stable. Based on the measurement, the calculated radiometer sensitivity is 1.7 K with 500 ms integration time. At 1930 MHz, the theoretical radiometer sensitivity due to IF bandwidth, integration time, and system noise temperature of 638 K (from Fig. 4.9) is 0.6 K (Eq. (2.23)). Rearranging Eq. (2.25) and then substituting into Eq. (2.24), the radiometer sensitivity due gain fluctuations is
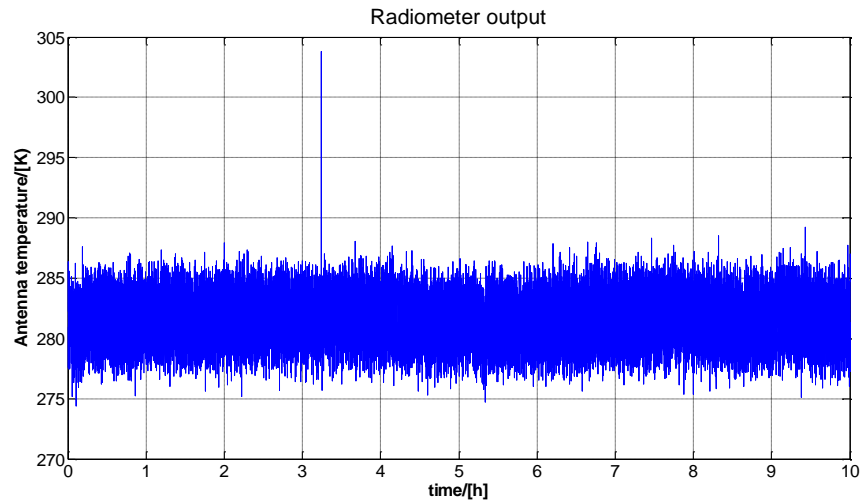
Figure 4.11. Radiometer output with 500 ms integration time and at 1930 MHz. Measurement was performed in a temperature controlled laboratory room.

$$\Delta T_G = \sqrt{\left(\Delta T\right)^2 - \frac{T_{SYS}^2}{B\tau}} = 1.6 \text{ K}. \tag{4.10}$$

4.6 Radiometer operation

The radiometer operation is tested by controlling the radiometer by the operating PC. The used PC has a Linux operating system, on top of which the purpose-built LIME-program runs. The use of the LIME-program is described in a software manual [53]. Actual measurements are performed by writing a Linux shell script, which then calls the LIME-program to perform a certain amount of measurements at a desired frequency, with specific input switch settings, etc. [54]. The output data is formatted into text

Figure 4.12. FIRaL radiometer.

files, which can then be processed further with mathematical software tools such as MATLAB. No serious hardware or software errors were detected during the laboratory tests. Fig. 4.12 shows the radiometer system during the laboratory tests.

5 On-site measurements

On-site measurements are performed in two locations in Espoo. The radiometer calibration is performed with external loads. The hot load is a microwave absorber plate at ambient temperature, which is placed in front of the horn antenna and sky is used as the cold calibration load. As with the laboratory calibration, the measurement uncertainty cannot be reliably determined and the measurement results have to be analysed accordingly. It is, however, possible to observe whether the measurement band is free of radio interference. Clear signal peaks are either emissions from mobile stations or possibly of interference origin.

5.1 Measurements in Otaniemi

Initial tests are conducted on the roof of the Department of Radio Science and Engineering in Otaniemi, Espoo. Possible radio interference is searched by measuring the environment by pointing the antenna horizontally towards each of the eight main points of compass. Fig. 5.1 shows the results of a frequency sweep while the antenna is pointed towards north. The peak at around 1930 MHz is most likely a signal from a mobile WCDMA2100-station and therefore not interference. No other signal peaks are visible above the noise floor in any directions. The measurements were performed
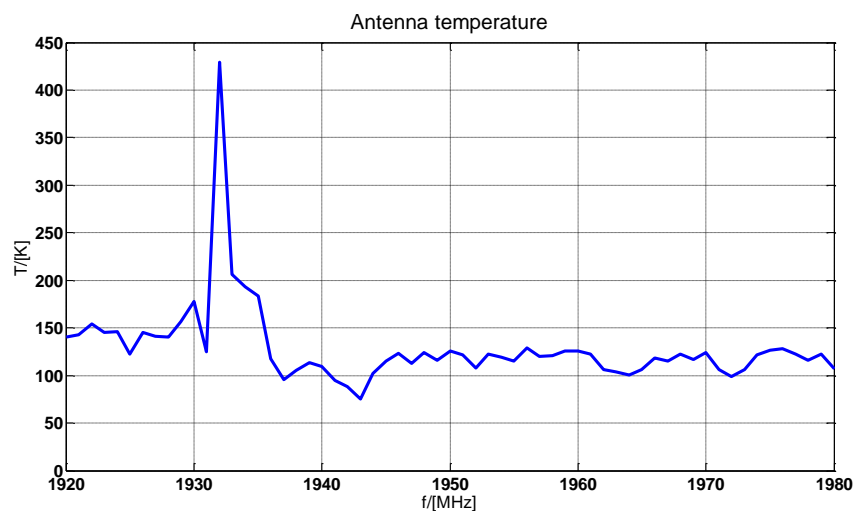

Figure 5.1. Radiometer output as function of frequency while looking towards north. Measurement integration time is 10 s.

during weekend, which might be a contributing factor to the absence of interfence as the operation of electric devices is at a minimum.

5.2 Measurements in Säteri

The second location is a rooftop of an NSN office building in Säteri, Espoo. Typical measurement responses are shown in Fig. 5.2. Both responses show severe interference components, which are at around 1958 MHz in the eastern direction and around 1975 MHz in the north-eastern direction. Measurements are performed during office hours. Corresponding views in the visible spectrum are shown in Fig. 5.3. Fig. 5.2 shows the full scale results. They show very high peak values from 13000 to 24000 K. The peaks may be uncontrolled mobile stations that are nearby, but there is also some probability that the signals are interference, because the high peaks in Fig. 5.2 have unequal
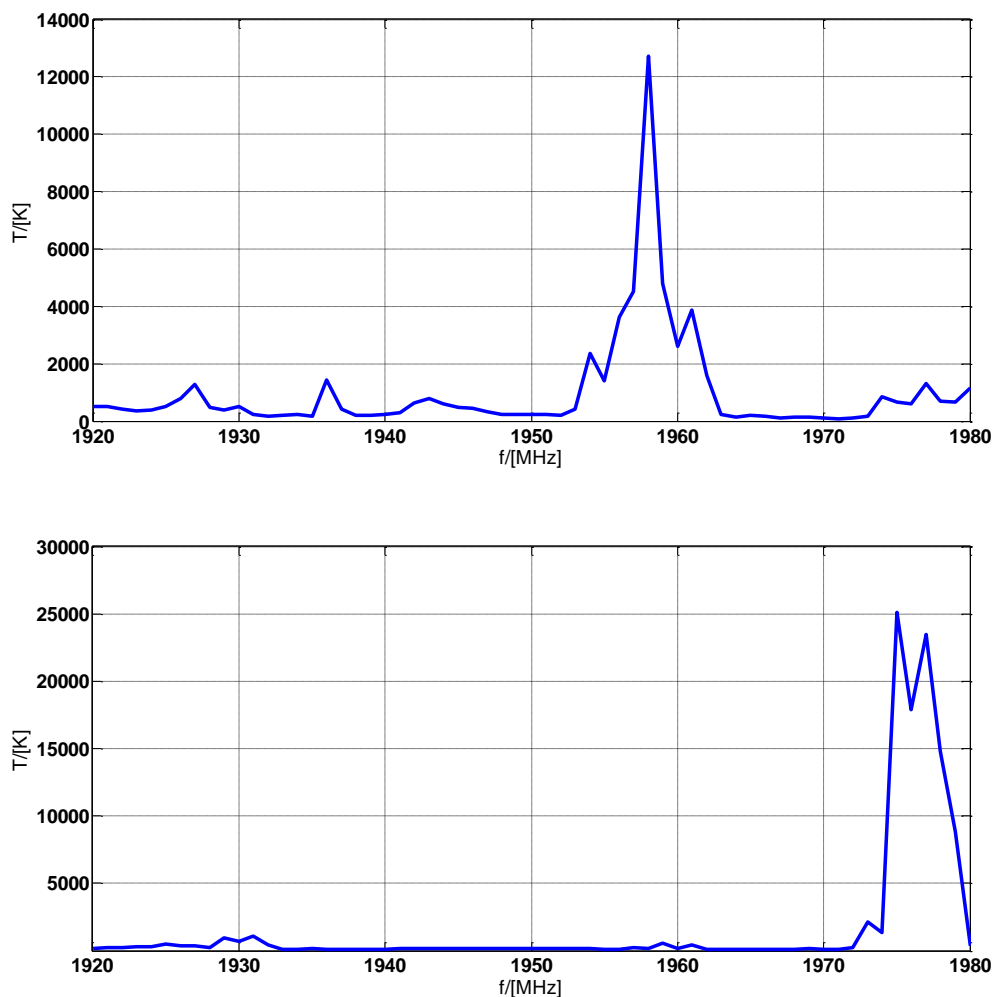
Figure 5.2. Radiometer output as function of frequency while looking towards east (upper) and north-east (lower). Measurement integration time is 10 s

<div align="center">(a)   (b)</div>

Figure 5.3. Visible spectrum views towards east (a) and north-east (b).

bandwidths in different viewing directions. A mobile station signal has a stable bandwidth of approximately 5 MHz.

The eastern view in visible spectrum in Fig. 5.3 (a) shows an office building that, of course, is a source of mobile signals. It can also be a source of interference, potentially arising from computer and communication systems, lightning and inverter driven aircon and ventilation systems.

Fig. 5.4 shows the same measurements as those in Fig. 5.2, but with a reduced brightness temperature scale in order to study the signals outside the very high peaks. The view towards east in Fig. 5.4 shows a number of signals from 500 to 1400 K. Some of those can be explained by mobile traffic, but not all. It is difficult to distinguish which of them are caused by mobile stations and which are interference. That would require longer measurements and more detailed analysis, which are beyond the scope of these preliminary measurements.
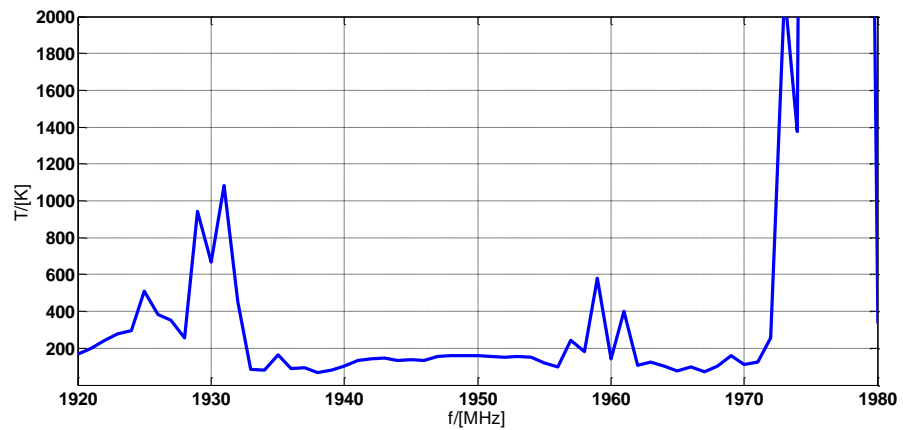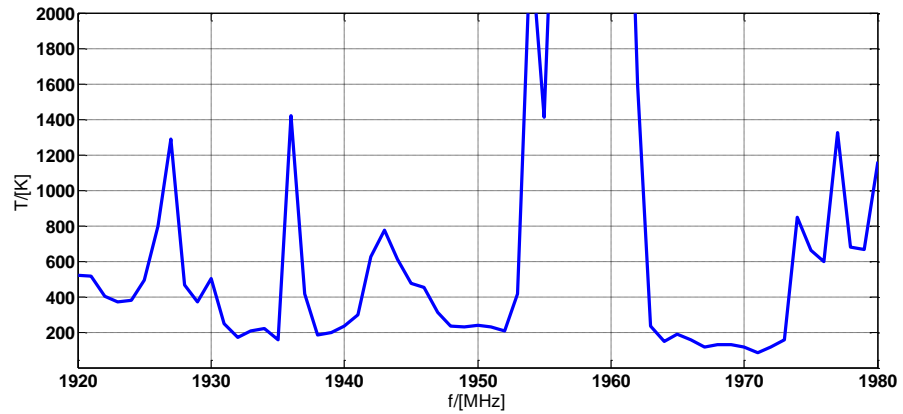
Figure 5.4. Closeups of the measured noise spectrums towards east (upper) and north-east (lower).

Fig. 5.5 shows the time variation of brightness temperature levels. It is not possible to reliably separate between mobile station signals and interference based on Fig. 5.5 either. Stable low level signals are most probably interference, while low level fluctuating signal are quite possibly mobile stations. High level peaks are also fluctuating, but it does not exclude the possibility that they could be also of interference origin.
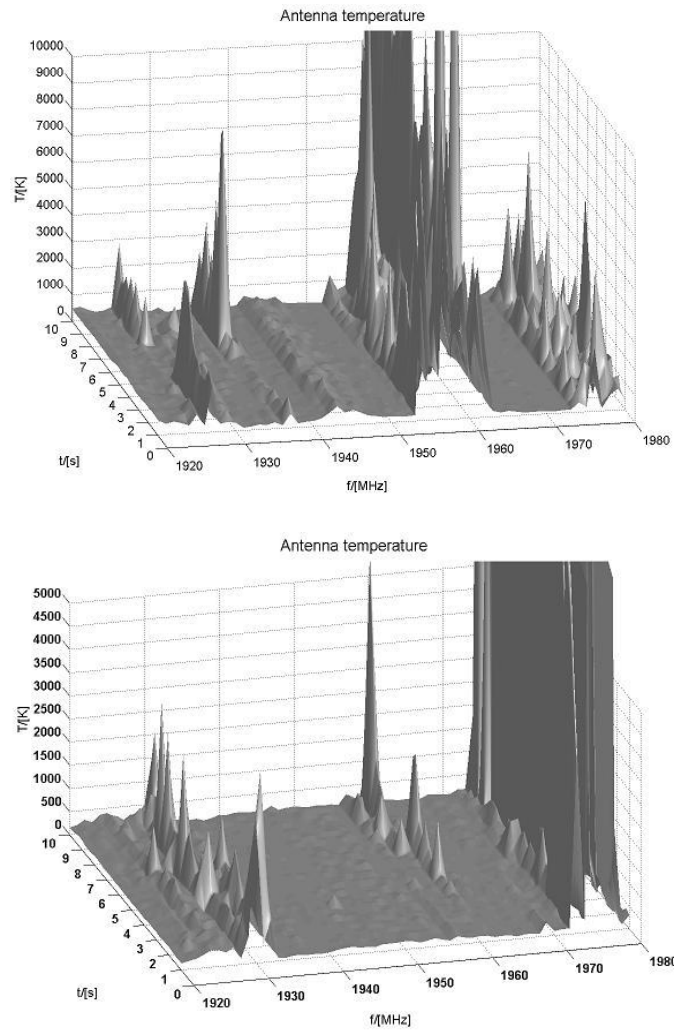
Figure 5.5. Radiometer responses as a function of time and frequency towards east (upper) and north-east (lower).

6 Conclusions

The FIRaL radiometer is completed within the constraints of the LIME project. A functional radiometer is designed and realised, and premiliminary on-site measurements have been performed. The measurement sensitivity of the radiometer is within the project specifications. The absolute measurement accuracy of the FIRaL radiometer cannot be defined to the precision which is usually associated with radiometers in general, due to the fact that the supplied RF amplifier components do not perform to the datasheet specifications. The realised receiver input noise temperature is 661 ± 58 K at the highest and 457 ± 76 K at the lowest in the radiometer operating band.

A redesigned RF amplifier section is needed in the radiometer receiver board before a comprehensive measurement campaign of actual WCDMA2100 base station locations is performed. The RF amplifier section unidealities also prevented the study and use of the most interesting feature of the FIRaL radiometer, namely the internal calibration loads and specifically the active cold load.

It is worth noting that a large bulk of this Licentiate work was spent on studying the RCB and TCB board electronics and software which are adopted from earlier radiometers developed in the Department of Radio Science and Engineering before they could be applied on the FIRaL radiometer. This somewhat tedious, but necessary work is not reported here as it is not interesting in terms of RF design or radiometry.

The results of the preliminary measurements in Säteri, Espoo suggest that the UMTS base station receiver band between 1920 – 1980 MHz could be seriously contaminated by radio interference and the concerns that gave rise to the LIME project in the first place are validated. It is necessary to find further funding in order to improve the RF amplifier performance and to perform additional measurements, which can then be reported in appropriate scientific publications.

References

[1]   European Communications Office, Copenhagen, Denmark, http://www.ero.dk/. [Accessed November 24, 2009].

[2]   FICORA, "Radio frequency regulation," Helsinki, Finland, 4 November 2009, http://www.ficora.fi/attachments/englantiav/5l1yqnUl7/RTM2009_englanti.pdf, [Accessed November 24, 2009].

[3]   L. B. Milstein, "Wideband code division multiple access," *IEEE Journal on Selected Areas in Communications*, Vol. 18, No. 8, pp. 1344-1354, Aug. 2000.

[4]   M. E. Tiuri, "Radio astronomy receivers," *IEEE Transactions on Antennas and Propagation*, Vol. 12, No. 2, pp. 930-938, 1964.

[5]   K. Rautiainen, J. Kainulainen, T. Auer, J. Pihlflyckt, J. Kettunen, and M. T. Hallikainen, "Helsinki University of Technology L-band airborne synthetic aperture radiometer," *IEEE Transactions on Geoscience and Remote Sensing*, Vol. 46, No. 3, pp. 717-726, 2008.

[6]   T. F. Ulaby, R. K. Moore, and A. K. Fung, *Microwave Remote Rensing – Active and Passive, Vol. I*, Addison-Wesley, 1981.

[7]   A. Räisänen and A. Lehto, *Radiotekniikan perusteet*, Helsinki: Otatieto, 2001.

[8]   E. A. Ohm and W. W. Snell, "A radiometer for a space communications receiver," *Bell System Technical Journal*, Vol. 42, pp. 2047-2080, 1963.

[9]   N. Skou and D. Le Vine, *Microwave Radiometer Rystems – Design and Analysis, 2nd edition,* Artech House, 2006.

[10]   J. Lemmetyinen, A. Colliander, K. Rautiainen, J. Kainulainen, S. Kemppainen, A. Aalto, and T. Auer, "L-band interference measurement in urban and suburban environments (LIME)," *Progress Report*, Tekes, 15 Dec. 2007, unpublished.

[11]   Y. H. Kerr, P. Waldteufel, J. –P. Wigneron, J. Martinuzzi, J. Font, and M. Berger, "Soil moisture retrieval from space: The Soil Moisture and Ocean Salinity (SMOS) mission," *IEEE Transactions on Geoscience and Remote Sensing*, Vol. 39, No. 8, pp. 1729-1735, Aug. 2001.

[12]   J. Kainulainen, K. Rautiainen, S. Tauriainen, T. Auer, J. Kettunen, and M. Hallikainen, "First 2-D interferometric radiometer imaging of the earth from an aircraft," *IEEE Geaoscience and Remote Sensing Letters*, Vol. 4, No. 2, pp. 241-245, Apr. 2007.

[13]   S. Kemppainen, J. Lemmetyinen, T. Auer, A. Colliander, A. Aalto, K. Rautiainen, and M. Hallikainen, "Thermal stabilized front-end PCB with active cold calibration load for L-band radiometer," *Proceedings of the IEEE International Geoscience and Remote Sensing Symposium*, Barcelona, Spain, 23-27 Aug., 2007, pp. 4433-4436.

[14]   R. H. Frater and D. R. Williams, "An active 'cold' noise source," *IEEE Transactions on Microwave Theory and Techniques*, Vol. MTT-29, pp. 344-347, Apr. 1981.

[15]   Mentor Graphics, OR, USA, http://www.mentor.com/. [Accessed Jan. 7, 2010].

[16]   A. Lehto and A. Räisänen, *RF- ja mikroaaltotekniikka*, Helsinki: Otatieto, 2001.

[17]   D. M. Pozar, *Microwave Engineering, 2nd Edition*, John Wiley & Sons, Inc., 1998.

[18]   The MathWorks, MA, USA, http://www.mathworks.com/. [Accessed Jan. 7, 2010].

[19]   Agilent Technologies, California, USA, http://www.home.agilent.com/agilent/home.jspx. [Accessed Jan. 7, 2010].

[20]   Analog Devices, Application Note AN 347.

[21]   Rogers Corporation, "RT/Duroid 6006/6010LM high frequency laminates," datasheet, 92-105, Jul. 2009.

[22]   Hittite Microwave Corrporation, "GaAs MMIC non-reflective switch, DC - 3.5 GHz," datasheet, v04.0404.

[23]   UBE Industries, "MD441 (under development)," datasheet, MD441-X1.

[24]   Richardson Electronics, "1700 ~ 2200 MHz super low noise amplifier," datasheet, 2005.

[25]   Maxim, Inc., "400MHz to 2500MHz SiGe ultra-low-noise amplifiers," datasheet, 19-1384 Rev. 2, Aug. 2003.

[26]   Maxim, Inc., "400MHz to 2.5GHz, low-noise, SiGe downconverter mixers," datasheet, 19-4786 Rev. 2, Aug. 2003.

[27]   Golledge Electronics, "SAW filter 70 MHz MA018181," datasheet, TB0194A Rev. No. 1.

[28]   Maxim, Inc., "DC-to-microwave, +5V low-noise amplifier," datasheet, 19-1135 Rev. 1, Aug. 2003.

[29]   Mini-Circuits, "Drop-in monolithic amplifier DC-3 GHz," datasheet, M108520 Rev. L, Jan. 2007.

[30]   Maxim, Inc., CA, USA, http://www.maxim-ic.com/. [Accessed Jan. 8, 2010].

[31]   Murata Manufacturing Co., Ltd., Japan. http://www.murata.com/. [Accessed Jan. 8, 2010].

[32]   Tusonix, "Surface mount square style pi filter," datasheet, X-2015 Rev. 0, Mar. 2005.

[33]   Philips Semiconductor, "74HC/HCT245 octal bus transceiver; 3-state," datasheet, IC06, Sep. 1993.

[34]   Rogers Corporation, "RO4000 series high frequency circuit materials," datasheet, 92-004, Apr. 2006.

[35]   Mini-Circuits, "Drop-in monolithic amplifier DC-3 GHz," datasheet, M108520 Rev. L, Jan. 2007.

[36]   AMI Semiconductor, "FS6377-01 programmable 3-PLL clock generator IC," datasheet, Nov. 2002.

[37]   Philips Semiconductor, "The I^2C-bus specification", Rev. 2.1, Jan. 2000. http://www.nxp.com/acrobat_download2/literature/9398/39340011.pdf. [Accessed Jan. 14, 2010].

[38]   R. P. Sallen and E. L. Key, "A practical method of designing RC active filters," *IRE Transactions on Circuit Theory*, Vol. CT-2, pp. 74-85, March 1955.

[39]   Daycounter, Inc., "Sallen-Key low pass filter calculator," UT, USA, http://www.daycounter.com/Filters/Sallen-Key-LP-Calculator.phtml. [Accessed Jan. 9, 2010].

[40] Motorola, "MC12179 500-2800 single channel frequency synthesizer," datasheet, MC12179/D Rev. 3, 1997.

[41] Circuit Sage, "Third order PLL Mathcad design routine," http://www.circuitsage.com/pll/pll3rd.pdf. [Accessed Jan. 11, 2010].

[42] Murata Manufacturing Co., "Chip EMIFIL LC combined type, NFW31SP series (1206 size)," datasheet, Apr. 2005.

[43] Flann Microwave, "Rigid rectangular waveguide data," http://www.flann.com/Products_Home/Components/FmiCat07122.pdf. [Accessed Jan. 12, 2010].

[44] G. Kordas, K. B. Baltzis, G. S. Miaris, and J. N. Sahalos, "Pyramidal-horn design under constraints on half-power beamwidth," *IEEE Antennas and Propagation Magazine*, Vol. 44, No. 1, pp. 102-108, Feb. 2002.

[45] C. A. Balanis, *Antenna Theory: Analysis and Design*, New York, John Wiley & Sons, Inc., 1997.

[46] Agilent Technologies, *8753ET/ES Network Analyzers Reference Guide*, Agilent Technologies, 2001.

[47] A. Lehto and A. Räisänen, *Mikroaaltomittaustekniikka*, Helsinki: Otatieto, 2001.

[48] M. Vaaja, "Design and realisation of instrumentation for a 650 GHz compact antenna test range," Diploma thesis, Teknillinen korkeakoulu, Espoo, Finland, 2006.

[49] *IEEE standard test procedures for antennas*, ANSI/IEEE Std 149-1979, 1979.

[50] W. L. Stutzman, "Estimating directivity and gain of antennas," *IEEE Antennas and Propagation Magazine*, Vol. 40, No. 4, pp. 7-11, Aug. 1998.

[51] Flann Microwave, "Standard gain horn model No. 0824-10, typical performance data," datasheet, Mar. 1995.

[52] P. Piironen, "PMS offset determination using an IF attenuator," ESA, Noordwijk, The Netherlands, May 16, 2002. Tech. Note.

[53] J. Pihlflyckt, *LIME-ohjelman käyttöohje*, Versio 1.1, 2009.

[54]   V. G. Gite, "Linux shell scripting tutorial v1.05r3, a beginner's handbook,"
http://www.freeos.com/guides/lsst/. [Accessed March 17, 2010].